

Review

Recent Advances in the Mitigation of the Catalyst Deactivation of CO₂ Hydrogenation to Light Olefins

Daniel Weber ^{1,†}, Tina He ^{2,†}, Matthew Wong ³ , Christian Moon ¹, Axel Zhang ⁴, Nicole Foley ¹, Nicholas J. Ramer ^{1,*} and Cheng Zhang ^{1,*}

- ¹ Chemistry Department, Long Island University (Post), Brookville, NY 11548, USA; Daniel.weber4@my.liu.edu (D.W.); Christian.moon@my.liu.edu (C.M.); nicole.foley2@my.liu.edu (N.F.)
² College of Natural Science, The University of Texas at Austin, Austin, TX 78712, USA; tinah00@utexas.edu
³ College of Engineering, Cornell University, Ithaca, NY 14850, USA; mcw243@cornell.edu
⁴ John Jay College of Criminal Justice, New York, NY 10019, USA; axel.zhang@jjay.cuny.edu
* Correspondence: nicholas.ramer@liu.edu (N.J.R.); cheng.zhang@liu.edu (C.Z.); Tel.: +01-516-299-3034 (N.J.R.); +01-516-299-2013 (C.Z.); Fax: +01-516-299-3944 (C.Z.)
† These authors contributed equally.



Citation: Weber, D.; He, T.; Wong, M.; Moon, C.; Zhang, A.; Foley, N.; Ramer, N.J.; Zhang, C. Recent Advances in the Mitigation of the Catalyst Deactivation of CO₂ Hydrogenation to Light Olefins. *Catalysts* **2021**, *11*, 1447. <https://doi.org/10.3390/catal11121447>

Academic Editors: Javier Ereña Loizaga and Ainara Ateka

Received: 10 November 2021
Accepted: 25 November 2021
Published: 28 November 2021

Publisher's Note: MDPI stays neutral with regard to jurisdictional claims in published maps and institutional affiliations.



Copyright: © 2021 by the authors. Licensee MDPI, Basel, Switzerland. This article is an open access article distributed under the terms and conditions of the Creative Commons Attribution (CC BY) license (<https://creativecommons.org/licenses/by/4.0/>).

Abstract: The catalytic conversion of CO₂ to value-added chemicals and fuels has been long regarded as a promising approach to the mitigation of CO₂ emissions if green hydrogen is used. Light olefins, particularly ethylene and propylene, as building blocks for polymers and plastics, are currently produced primarily from CO₂-generating fossil resources. The identification of highly efficient catalysts with selective pathways for light olefin production from CO₂ is a high-reward goal, but it has serious technical challenges, such as low selectivity and catalyst deactivation. In this review, we first provide a brief summary of the two dominant reaction pathways (CO₂-Fischer-Tropsch and MeOH-mediated pathways), mechanistic insights, and catalytic materials for CO₂ hydrogenation to light olefins. Then, we list the main deactivation mechanisms caused by carbon deposition, water formation, phase transformation and metal sintering/agglomeration. Finally, we detail the recent progress on catalyst development for enhanced olefin yields and catalyst stability by the following catalyst functionalities: (1) the promoter effect, (2) the support effect, (3) the bifunctional composite catalyst effect, and (4) the structure effect. The main focus of this review is to provide a useful resource for researchers to correlate catalyst deactivation and the recent research effort on catalyst development for enhanced olefin yields and catalyst stability.

Keywords: CO₂ hydrogenation; light olefins; catalyst deactivation; CO₂-Fischer-Tropsch (CO₂-FT); iron-based catalysts; methanol to olefins; bifunctional composite catalysts; SAPO-34

1. Introduction

1.1. General Aspects

While carbon-rich fossil fuels like coal, oil, and natural gas have powered human civilization, the massive emission of CO₂ as a greenhouse gas has caused severe and harmful effects on the ecological environment [1]. For example, the rise of sea levels is accelerating, the number of large hurricanes and wildfires is growing, and dangerous heat waves and more severe droughts are occurring in many areas. The CO₂ concentration in the atmosphere had climbed to 415 ppm by 2020 (Figure 1), an increase of more than 40% relative to the pre-industrial era [2]. The atmospheric CO₂ concentration will continue to rise to ~570 ppm by the end of the 21st century if no alleviation measures are taken [3]. Therefore, there is an urgent need to control CO₂ emissions in order to mitigate their negative impact on the environment. In recent years, capture and storage technologies for the CO₂ released from the burning of fossil fuels have emerged and developed in potential commercial scale applications [4–7]. In order to close the carbon gap, transforming the

captured gas into value-added fuels and chemicals has become an urgent task for CO₂ remediation [8,9].

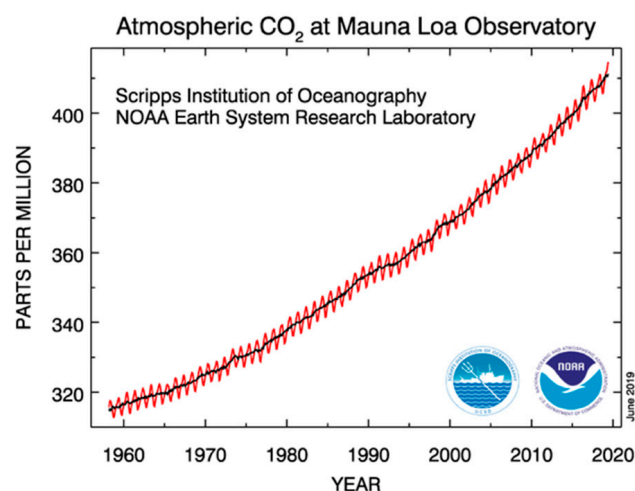
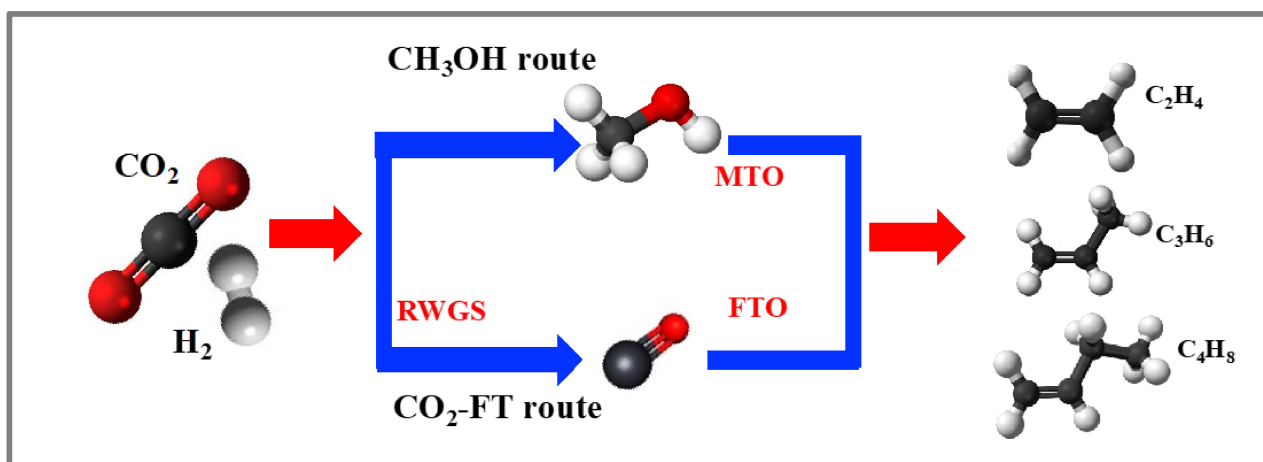


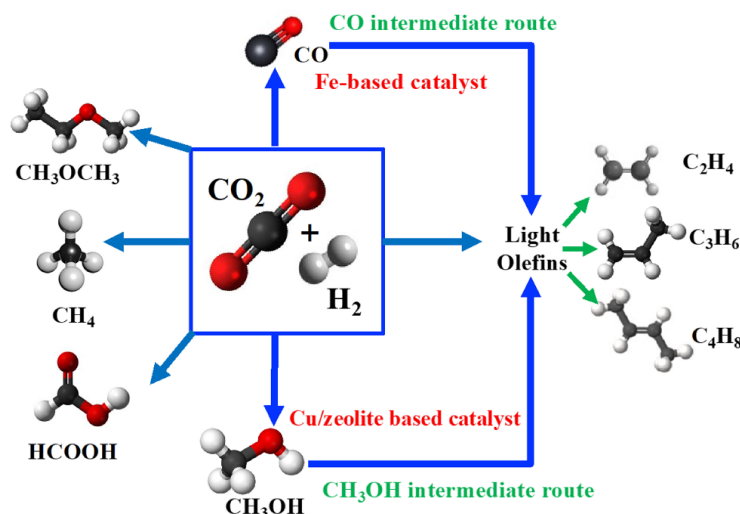
Figure 1. Trends in the atmospheric CO₂ concentration (ppm) [2].

The catalytic conversion of CO₂ is a favorable approach to the mitigation of CO₂ emissions by producing chemicals and fuels [8,10–17]. Light olefins such as ethylene, propylene and butylene (C₂–C₄), which are currently among the top petrochemicals, are the building blocks for the production of a wide variety of polymers, plastics, solvents, and cosmetics [8,13,18–21]. Moreover, light olefins can be oligomerized into long-chain hydrocarbons which can be used as fuels, making them a desirable product with high potential for the utilization—and therefore elimination—of up to 23% of CO₂ emissions [8]. A highly promising route is selective CO₂ hydrogenation to produce light olefins [10]. The huge market demand for the lower olefins offers a great opportunity for the target technology to profoundly impact the scale of CO₂ utilization once it is developed with renewable hydrogen. The current chemical industry relies heavily on petroleum (the steam cracking of naphtha) for the production of light olefins [22]. The depletion or movement away from the refining of petroleum and the gap between the supply and demand of light olefins call for a new strategy to synthesize light olefins from alternative carbon sources [18–21,23,24]. A one-step process for the conversion of CO₂ to light olefins is a highly desirable tactic to address the “3Rs” (reduce, reuse, and recycle) associated with ever-increasing CO₂ levels, and to solve the paradox between the supply and demand of light olefins [25].

Currently, there are two primary pathways, as shown in Scheme 1, to produce light olefins from CO₂ reduction by hydrogen (H₂) in a one-step process: (1) the CO₂ Fischer–Tropsch synthesis (CO₂–FTS) route consists of two consecutive processes, the reverse water–gas shift (RWGS) reaction (Equation (1)) and subsequent Fischer–Tropsch synthesis (FTS) (Equation (2)); (2) the methanol (MeOH) mediated route consists of two consecutive processes, i.e., CO₂-to-MeOH (Equation (3)) and a subsequent MeOH-to-olefins process (MTO) (Equation (4)). The complex reaction network in Scheme 2 indicates the competing reactions (i.e., Equation (5)) with the formation of light olefins. The control of the selectivity of the CO₂ hydrogenation to the desired olefin product requires the design of catalysts for reaction pathways that are compatible with favorable thermodynamics and a good understanding of the reaction kinetics [26]. The thermodynamic values in the equations (Equations (1)–(5)) indicate that lower temperatures favor FTS (Equation (2)), methanol (Equation (3)), and methane synthesis (Equation (5)), while higher temperatures are needed to activate CO₂ (Equation (1)) for rapid reaction rates [27]. The complex reaction network in Scheme 2 and thermodynamics suggest that the design and synthesis of catalysts for a one-step process to selectively produce olefins are challenging.



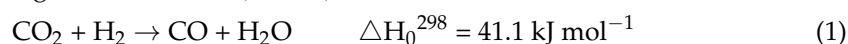
Scheme 1. Reaction route for CO₂ hydrogenation to light olefins.



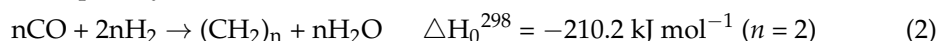
Scheme 2. Complex reaction network for CO₂ conversion to chemicals through hydrogenation.

CO₂-FTS reaction pathway:

Reverse water-gas shift reaction (RWGS):

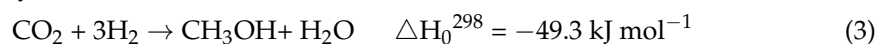


Fischer-Tropsch synthesis to olefins (FTS):

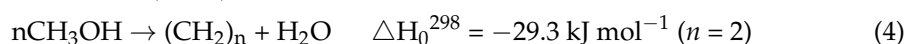


Methanol mediated reaction pathway:

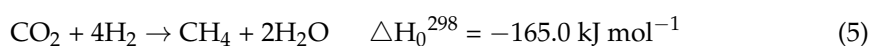
Methanol synthesis:



Methanol to olefins (MTO):



CO₂ methanation:

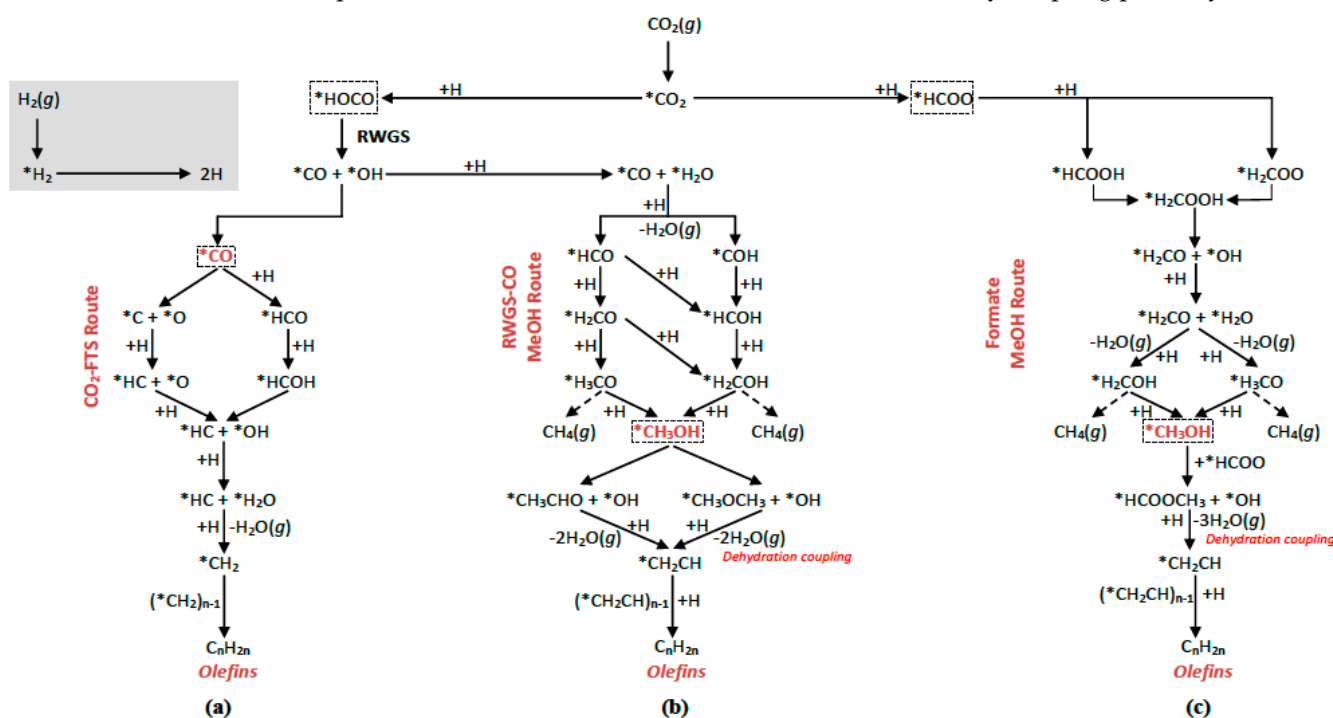


1.2. Mechanistic Insights for CO₂ Conversion to Light Olefins

In reviewing the mechanistic details of the light olefin formation, it is clear that controlling the active H to C ratio is of primary importance. The presence of too much H* on the surface will result in excessive hydrogenation, and therefore methanation, while too little H* on the surface will restrict the hydrogenation ability of the catalyst and

therefore reduce the CO₂ conversion activity. At its most fundamental, the pivotal steps of CO₂ conversion to light olefins are the cleavage of the C–O bonds and the formation of C–C bonds [25].

Iron-based catalysts have been extensively studied for use in the CO₂–FTS route due to their relatively high utility and activity for both the RWGS and FTS component reactions. When using Fe-based catalysts for CO₂–FTS, the initial Fe₂O₃ phase is reduced by hydrogen to Fe₃O₄ or a mixture of Fe₃O₄ and FeO. The resulting Fe₃O₄ is the active component for the RWGS reaction, and can be further reduced to form metallic Fe [27]. The reaction mechanism for the CO₂–FTS pathway is suggested as shown in Scheme 3a. CO₂ is first adsorbed and activated on the RWGS active phases (e.g., Fe₃O₄) to form a carboxylate (*CO₂, * representing the adsorption state). The *CO₂ can then be hydrogenated by adsorbed H to form an *HOCO intermediate. The intermediate then dissociates into *OH and *CO. The *OH is then hydrogenated into *H₂O. Then, *CO either desorbs as CO gas or reacts further via successive FTS. In order to form hydrocarbons, the *CO is first partially hydrogenated into *HCO and then undergoes complete hydrogenation, dissociation, and finally dehydration to form *CH_x species. The *CH_x species are precursors for the formation of olefins. In an alternative mechanism, *CO can dissociate into *C and *O. Some *C can diffuse into the Fe-metal lattice to form metal carbides as χ -Fe₅C₂, the active component for the FTS reaction [27]. The C* on the χ -Fe₅C₂ surface can then be hydrogenated to CH_x* species. C* + CH_x* and CH_x* + CH_x* were the most likely coupling pathways [25].



Scheme 3. (a–c) Reaction mechanism for CO₂ hydrogenation to light olefins (modified and adapted with permission from ref. [27]. Copyright 2021 Elsevier).

As indicated above, the *C from the dissociation of *CO during the FTS reaction may diffuse into the α -Fe metal lattice, resulting in the formation of Fe₇C₃, χ -Fe₅C₂, θ -Fe₃C, ϵ' -Fe_{2.2}C, and ϵ -Fe₂C phases, depending on reaction conditions [27]. Iron carbides play an essential role in CO hydrogenation/dissociation and C–C coupling. Some researchers have proposed that χ -Fe₅C₂ is the active phase, while θ -Fe₃C is less active and can cause catalyst deactivation due to production of graphite, which has increased stability under typical FTS reaction conditions and may block the production of other active phases [27,28].

Alternatively, the reaction mechanism for the MeOH pathway is suggested as shown in Scheme 3b,c. The synthesis of MeOH can proceed via two pathways: (1) CO-mediated, in which the *CO intermediate, which was produced from the RWGS reaction via the

dissociation of the carboxyl (*HOCO) species, is hydrogenated to methanol via *HCO and *COH , and (2) formate-mediated, in which the formate (*HCOO) species results from the hydrogenation of the carboxylate intermediate (*CO_2), which is then reacted further to *H_2COOH , *H_2CO , *H_2COH , and *H_3CO . Through dehydration coupling, the methanol forms *CH_2CH , and then forms olefins via subsequent hydrogenation [27].

The factors that may affect the CO_2 conversion and light olefin selectivity are the catalyst composition (metals, supports, promoters, etc.), functionality (i.e., metal/zeolite bifunctionality), structure (i.e., layered metal oxide, core-shell, etc.), preparation methods (e.g., impregnation, hydrothermal, sol-gel, etc.) and testing conditions (e.g., temperature, pressure, CO_2/H_2 molar ratio, gas hourly space velocity, etc.). The focus of this review will be on the catalyst composition, functionality and structure. Other factors of catalyst preparation methods and testing conditions for CO_2 conversion to light olefins can be found elsewhere [15,20,27,29,30].

1.3. Catalysts for CO_2 Conversion to Light Olefins

As can be seen above, because each route has its own unique pathway of species and intermediates, different catalysts must be employed for the hydrogenation of CO_2 to olefins depending on the chosen route. In the CO_2 -FTS path, Fe is one of the most widely used components in the catalysts, as catalysts containing Fe offer less methanation activity under higher reaction temperatures. As described above, it has been reported that Fe_3O_4 was the active phase responsible for RWGS; the metallic Fe and iron carbides could activate CO and produce hydrocarbons [31,32]. When incorporating alkali promoters, Fe-based catalysts showed greater olefin selectivity. The alkali metals, acting as electron donors to the Fe metal, facilitate the adsorption of CO_2 while lowering the affinity for H_2 . The net result is a higher olefin yield [33–35]. There is also some indication that doping the catalyst with an additional metal may promote even higher olefin yields by forming a highly active interface. The second metal components allow for even greater adjustment of the CO_2 and H_2 adsorption and activation, shifting the distribution of the product more towards the desired hydrocarbons. By supporting the Fe-based catalysts on supports such as silica (SiO_2), alumina (Al_2O_3), titania (TiO_2), zirconia (ZrO_2) and carbon materials (i.e., carbon nanotubes (CNTs), carbon nanospheres (CNSs), graphene oxide (GO)), the catalytic performance may be further enhanced by improving the active metal dispersion and slowing down the sintering of the active particles [36,37]. Controlling hydrocarbon chain growth to achieve a desired carbon range (i.e., C_2 – C_4) remains a challenge for CO_2 conversion due to the product selectivity limit governed by the Anderson–Schulz–Flory (ASF) distribution with a maximum achievable C_2 – C_4 hydrocarbons selectivity of less than 60%, as shown in Figure 2 [30,38].

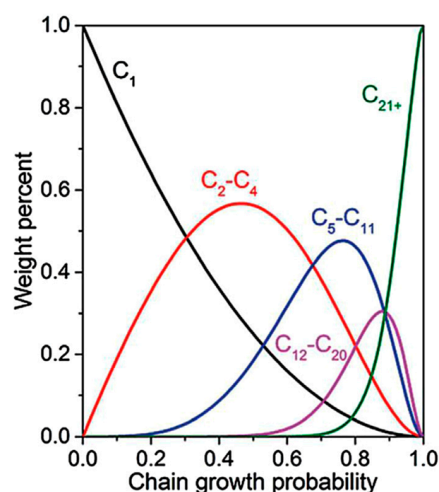


Figure 2. Product distribution as predicted by the Anderson–Schulz–Flory (ASF) model. Adapted with permission from ref. [30]. Copyright 2021 Elsevier.

Alternatively, in the MeOH path, light olefins can be synthesized with selectivity as high as 80–90% among hydrocarbons, exceeding the ASF product distribution limit for FTS reactions [18,39–41]. Some plausible reasons for the reported ASF distribution deviation are the blockage of surface polymerization by intermediates, (e.g., ketene (CH_2CO)), space confinement, or the use of catalysts with two types of active sites (i.e., bifunctional catalysts) [27]. Regardless of the reasons, the observed deviation from the ASF distribution offers opportunities to increase the selectivity to olefins [27]. Several recent studies have reported the results for the combination of MeOH synthesis catalysts (i.e., In_2O_3 , In-Zr, ZnGa_2O_4 , MgGa_2O_4 , ZnAl_2O_4 , MgAl_2O_4 , ZnZrO and In_2O_3 -ZnZrO₂) with an MTO catalyst (i.e., SAPO-34, SSZ-13 and ZSM-5), and their ability to produce light olefins with enhanced selectivity for CO_2 hydrogenation [13,42–44]. It has been proposed that the secondary functionality of acid–base sites on the catalytic support significantly impacts the light olefin selectivity. For example, by passivating the Brønsted acid sites of In_2O_3 -ZnZrO_x/SAPO-34, the secondary hydrogenation reaction is inhibited, thereby improving the olefin selectivity [27,30].

1.4. The Main Focus of This Review

Even though significant efforts have been made, considerable challenges remain in the development of highly efficient catalysts with selective pathways to light olefins due to the thermodynamically stable nature of the CO_2 molecule, the complexity of the reaction networks, and catalyst deactivation [8,45,46]. Several recent reviews have summarized CO_2 hydrogenation to value-added products, including light olefins [25,27,30,38]. However, it is necessary to present a review focused on the recent advances in the mitigation of the catalyst deactivation of CO_2 hydrogenation to light olefins, as catalyst deactivation has been a big challenge that provides economic hurdles to the adoption of the new technologies.

Because catalysts and mechanisms have been extensively reviewed in numerous review papers [25,27,30,38], the focuses of the current article are to identify possible causes that trigger catalyst deactivation and summarize recent advances on catalyst development with enhanced catalyst stability and light olefin selectivity for CO_2 hydrogenation. In this review, we first provide a brief summary of the two dominant reaction pathways (CO_2 -FTS and MeOH-mediated), mechanistic insights and catalytic materials for CO_2 hydrogenation to light olefins. We then list the deactivation mechanism caused by carbon deposition, water formation, phase transformation and metal sintering/agglomeration. Finally, we summarize the recent progress published within five years on catalyst development that improves catalyst deactivation by the following catalyst functionalities: (1) the promoter effect, (2) the support effect, (3) the hybrid functional effect, and (4) the structure effect.

Each one of these aspects is accompanied by a suitable table in which the most significant literature findings are comparatively presented. To the best of our knowledge, no review has ever directly correlated the causes of catalyst deactivation and catalyst mitigation for CO_2 hydrogenation to light olefins. Herein, we attempt to provide a useful resource for researchers to correlate the catalyst deactivation and the recent research effort on catalyst development for enhanced olefin yield and catalyst stability.

2. Causes of Catalyst Deactivation

During CO_2 hydrogenation, catalyst deactivation can occur via several mechanisms, resulting in decreased activity and selectivity toward the desired olefins. The determination of the mechanism of deactivation is an important step toward mitigation. The primary causes of catalyst deactivation are the sintering (or agglomeration) of metal particles, phase transformation at the catalyst's surface, and catalyst poisoning by water or carbonaceous deposits (i.e., coke). An understanding of the deactivation causes is necessary to develop a mitigation strategy and sustain high selectivity toward the desired olefins during CO_2 hydrogenation. For context, we present brief descriptions of each of these causes with a few representative examples from the literature that demonstrate the necessity of robust

and novel mitigation studies. More thorough reviews of the deactivation causes and their mechanisms can be found elsewhere [47–49].

2.1. Sintering

Catalyst sintering can occur through either Ostwald ripening or particle migration and coalescence, as shown in Figure 3 [50]. Through sintering, the agglomeration of smaller catalyst crystals into larger ones will bring about the loss of the pore structure, which lowers the internal surface area of the catalyst, leading to the deactivation. In the area of FT by cobalt catalysts, several groups have determined that the particle growth of cobalt is the largest factor causing deactivation [51,52].

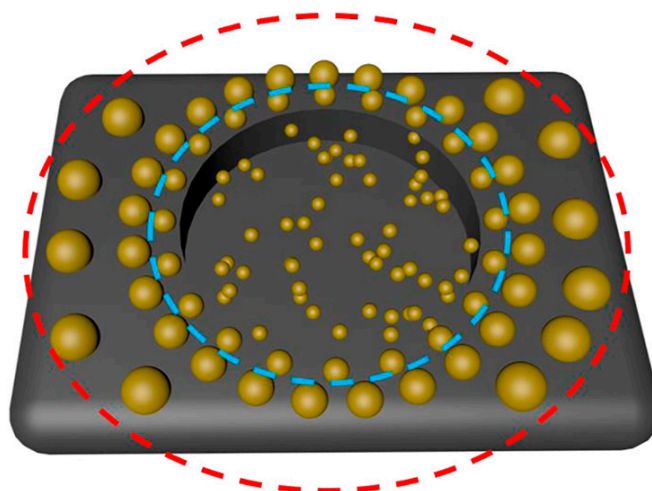


Figure 3. Diagram of active phase sintering occurring over a support material: the blue ring represents atomic migration to form larger crystallites; the red ring represents the coalescence of crystallites. Adapted with permission from ref. [50]. Copyright 2021 Elsevier.

Sun et al. [53] examined sintering in zinc- and alumina-supported copper catalysts ($\text{Cu}/\text{ZnO}/\text{Al}_2\text{O}_3$). It was found that the presence of CO in the process employed for CH_3OH synthesis strongly contributed to the deactivation of the catalysis over 0 to 50 h. Taken with corroborative evidence from the Cu surface area determination, the deactivation was likely attributed to the sintering of the Cu metal.

As mentioned above, sintering negatively affects the catalytic performance due to many reasons: for example, the overall catalytically active surface area is reduced due to the collapse of the structure and the chemical alteration of the catalytically active phases to non-active phases [50,54,55]. As this form of deactivation involves the coalescence of larger particles from smaller, it is extremely difficult to reverse. Sintering, therefore, is easier to prevent through careful catalyst design [50,56]. For example, Li et al. observed remarkable metal sintering on supported FeCo/ZrO_2 catalysts [56]. As shown in Figure 4A(a), for the $^{13}\text{Fe}_2\text{Co}/\text{ZrO}_2$ supported catalyst precursor prepared using the conventional impregnation method, the Co and Fe are distributed into separate oxide particles, which increased the possibility of sintering. As confirmed in Figure 4A(b,c), aggregates composed of Fe and Co oxide nanoparticles were observed on the ZrO_2 fibers, with an average diameter of ca. 15 nm before the reaction. The particle size increased to 48 nm after the reaction, which was responsible for the rapid deactivation of activity (Figure 4A(d–f)). By comparison, Fe-Co-Zr polymetallic fibers obtained via a one-step electrospinning technique showed that Fe and Co were dispersed in proximity to ZrO_2 , as shown in Figure 4C(a), but separately from each other. In order to reduce the possibility of sintering, as demonstrated in Figure 4B(a–f), the Fe and Co oxides nanoparticles successfully dispersed with the ZrO_2 particles for the polymetallic oxide fibers, with an average size of roughly 1–2 nm before the reaction, and after the reaction, the particle size barely changed, which contributed to the stable catalytic activity after 500 mins on stream (Figure 4C(a,b)).

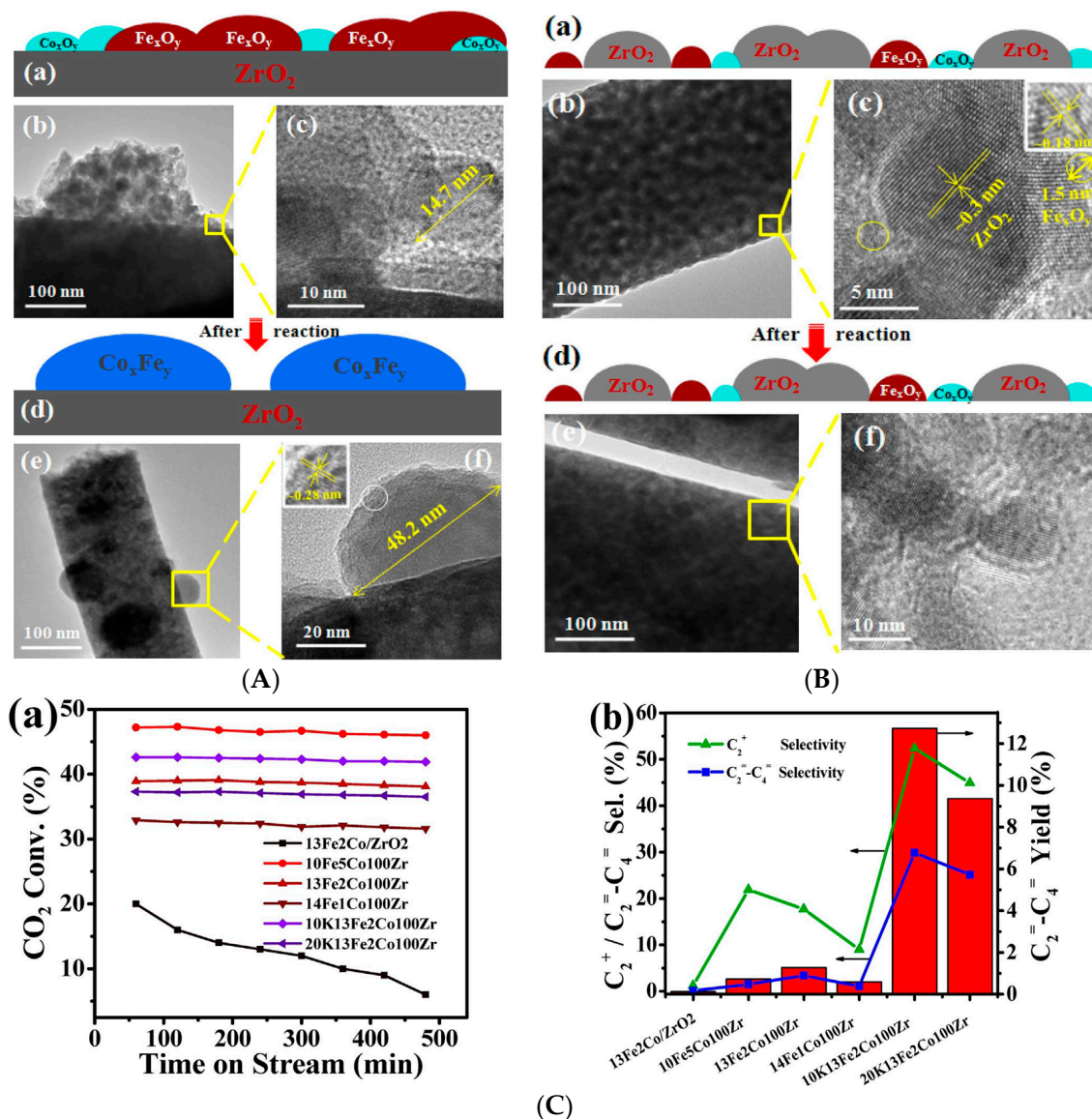


Figure 4. (A) (a–f) Schematic illustration of the metal distribution and TEM images of the 13Fe₂Co/ZrO₂-supported catalyst precursor (a–c) and the spent catalyst (d–f). (B) (a–f) Schematic illustration of the metal distribution and TEM images of the 13Fe₂Co100Zr polymeric oxide fiber catalyst (a–c) and the spent catalyst (d–f). (C) CO₂ conversion (a) and the C₂₊/C₂⁼-C₄⁼ selectivity and C₂⁼-C₄⁼ yield (b) over different catalysts after 8 h TOS (testing conditions: H₂/CO₂ molar ratio = 3/1, GHSV = 7200 mL g⁻¹ h⁻¹, P = 3 MPa, T = 673 K). Adapted with permission from ref. [56]. Copyright 2019 Elsevier.

2.2. Phase Transformations

Phase transformations are processes of deactivation involving the conversion of an active crystalline phase of the catalyst (or one of its components) into a different inactive one. These transformations can involve both metal-supported and metal-oxide catalysts. In the former type of catalyst, atoms from the catalyst's support will diffuse into the catalyst's surface. A reaction at the surface can then result in an inactive phase, deactivating the catalyst.

Riedel et al. was able to demonstrate that the steady states of the synthesis of hydrocarbons using iron oxides could be separated into five episodes of distinct kinetic regimes. In episode I, the adsorption of the reactants takes place on the catalyst surface and carbonization occurs. During episodes II and III, products from the RWGS reaction dominate during ongoing carbon deposition. In episode IV, the rate of FT activity increases up to the steady

state, and the maintenance of the steady state occurs in episode V. Prior to the reaction, the iron phases of the reduced catalyst are mainly α -Fe and Fe_3O_4 , along with a small amount of Fe_2O_3 . As the process proceeds, the Fe_3O_4 and Fe_2O_3 phases are consumed and a new oxidic iron amorphous phase is formed, which appears to be active for the RWGS reaction. Through a reaction of iron with carbon from the CO dissociation, FTS activity commences with the formation of iron carbide (Fe_5C_2). Upon the formation of the stable but inactive carbide (Fe_3C), which is the result of Fe_5C_2 carburization, the catalyst begins deactivating [57–59]. Lee et al. studied the causes of the deactivation of Fe-K/ γ - Al_2O_3 for CO_2 hydrogenation to hydrocarbons, and found the causes for deactivation varied based on positioning inside the reactor. Over time, the Fe_2O_3 was reduced to active phase χ - Fe_5C_3 , and then the χ - Fe_5C_3 was transformed to θ - Fe_3C , a form which is not active for CO_2 hydrogenation. The primary reason for deactivation was the phase transformation at the top of the reactor. Conversely, at the bottom of the reactor, deactivation was largely the result of deposited coke generated by secondary reactions [57].

Zhang et al. reported the structure evolution of the iron catalyst during its full catalytic life cycle of CO_2 to olefins (CTO), including the catalyst activation, reaction/deactivation (120 h) and regeneration. The phase transition during the CO activation was observed to follow the sequence of $\text{Fe}_2\text{O}_3 \rightarrow \text{Fe}_3\text{O}_4 \rightarrow \text{Fe} \rightarrow \text{Fe}_5\text{C}_2$. The primary deactivation mechanism during CTO was identified as the irreversible transition of iron phases under reaction conditions. Two possible pathways of the phase transition of the iron catalyst under CTO conditions have been identified, i.e., $\text{Fe}_5\text{C}_2 \rightarrow \text{Fe}_3\text{O}_4$ and $\text{Fe}_5\text{C}_2 \rightarrow \text{Fe}_3\text{C} \rightarrow \text{Fe}_3\text{O}_4$. Moreover, carbon deposition and the agglomeration of the catalyst particle proves to have relatively minor impacts on the catalytic activity compared with phase transition during the 120 h of reaction [60].

It appears that transformation to iron oxides will destroy catalyst activity. There is some question as to whether the cementite phase itself is problematic to activity, as higher-surface-area cementite phases have been reported to perform CO_2 hydrogenation quite effectively [61].

2.3. Poisoning

Catalytic poisoning is a result of the strong chemisorption of reactants, products or impurities on sites that would otherwise be capable of catalysis. In essence, the poisoning ability of a particular species is related to the strength of its chemisorption to the catalysis relative to the other reactants that are competing for the catalytic active sites. The poisoning has two deactivating effects; a poison physically blocks the active sites from receiving additional reactants, and a poison can alter the electronic or structural properties of the catalytic surface, rendering it partially or completely ineffective toward catalysis [62,63].

While there are several different poisons which have been reported in the literature that have shown to deactivate CO_2 hydrogenation catalysts [64,65], we will focus on the two which are the most pervasive, namely water and carbonaceous deposits or coke.

2.3.1. Water Poisoning

As seen in the above CO_2 hydrogenation reactions, the dissociation of CO_2 produces oxygen atoms, which in turn results in the formation of water. This byproduct is necessary for the thermodynamic favorability of the entire process, but can be unfortunately detrimental to catalytic performance. It is because of this unavoidable mechanistic absolute that the mitigation of water poisoning must be part of all catalytic investigations [66].

Wu et al. [67,68] examined the effect of the produced water on the stability of Cu/ZnO-based catalysts in methanol synthesis from the high temperature hydrogenation of CO_2 . Specifically, Cu/ZnO/ZrO₂/Al₂O₃ (40/30/25/5) was subjected to a CO_2 -rich feed, which produces water, and a CO-rich feed, which does not produce water. The examination of the catalysts by X-ray powder diffraction (XRD) after 1 h and 500 h time-on-stream of a CO_2 -rich feed containing steam showed that the Cu and ZnO crystallized more rapidly when compared to identical catalysts exposed to a CO-rich feed not containing steam.

In particular, the Cu particle size in the catalyst used with the CO₂-rich feed containing steam grew from 94 Å to 166 Å from 1 h to 500 h. The particle size growth under steam might be the key reason causing catalyst deactivation.

Huber et al. observed the rapid deactivation of Co/SiO₂ during an FTS reaction at high water partial pressure, and the loss of activity was attributed to the support breakdown byproduct water accompanied by the formation of stable, inactive cobalt-silicates and the loss of the BET surface area [69]. van Steen et al. stated that metallic cobalt crystallites with a diameter less than 4.4 nm are more susceptible to oxidation by water to form Co(II)O [70]. This is in agreement with Iglesia's work showing that small Co metal crystallites (<5–6 nm diameter) appear to re-oxidize and deactivate rapidly in the presence of a water reaction product in typical FTS conditions [71].

Water poisoning has the most dramatic effect on zeolite-based CO₂ hydrogenation catalysts for which the acidic sites of the zeolite are essential for catalysis. Recently, Zhang et al. investigated the water effect over zeolite-based catalysts at high temperatures, and found that water caused the loss of crystallinity and modified acid sites, thereby deactivating the catalyst [72]. Their studies show, by functionalization with organosilanes, that the tolerance of defective zeolites to hot liquid water can be greatly enhanced. This method renders the zeolite hydrophobic, which prevents the wetting of the surface. At the same time, the organosilanes act as a capping agent of Si–OH species, reducing their reactivity. Both aspects are important for the prevention of water attack [72].

It appears that there are several analogies of Fe catalysts for CO₂ hydrogenation and CO catalysts for conventional FT synthesis. Kliewer et al., for example, showed that for a supported CO catalyst, water can oxidize the surface of the CO to an inactive oxide phase, and it also plays a large role in sintering. With a high water partial pressure in the Fe system, it appears that this can also oxidize iron carbides to inactive surface oxide phases and also promotes particle growth sintering [51].

2.3.2. Carbonaceous Deposits (Coke)

Coke is produced by the decomposition or condensation of hydrocarbons on the surfaces of catalysts, and is primarily comprised of polymerized hydrocarbons. There have been several books and reviews that describe the formation of coke on catalysts, and the resulting deactivation [73–78].

These deposits are most problematic for catalysis involving zeolites, because the active sites of the zeolites become blocked or fouled by the coke deposits. The deactivation of MTO reactions over zeolites due to coke deposition results in a reduction in both the catalyst activity and product selectivity [79–81].

Nishiyama et al. [82] studied the effect of the SAPO-34 crystal size on the catalyst lifetime, and found that the amount of coke deposited on the deactivated SAPO-34 catalyst increased with the decreasing crystal size, indicating that for larger crystals, the reactants were unable to penetrate further into the larger crystals to reach other acidic sites. Because MTO reactions and coke formation take place simultaneously in the same pores, it seems likely that the effectiveness of the catalyst increased with the decreasing crystal size. Their studies demonstrated that the coke formation was inhibited in small-crystal SAPO-34 due to reduced diffusive resistance.

The work of Wei et al. on CO₂ hydrogenation found that the deactivation of the zeolites Hmcm-22 and HBeta was the result of coke formation, which deposited in the zeolites' cavities and channels. The deposition blocked the reactants' access to the zeolites' acid sites, leading to the deactivation [11]. Muller et al. investigated the MTO process on H-ZSM-5 catalysts in plug-flow (PFR) and fully back-mixed reactors (CSTR). They found that the catalysts deactivated under the homogeneous gas phase in the CSTR. It was shown unequivocally that, in the early stages of the reaction, the zeolite deactivates via Brønsted acid site blocking, and not by coke-induced deposition restricting the pore access. The deactivation of H-ZSM-5 in the CSTR occurred at first rapidly, and then at a much slower rate (Figure 5). The rapid deactivation was observed in a PFR due to the

formation of a larger fraction of the oxygen-containing carbon species. The larger fraction of oxygen-containing carbon species increases the reaction with the desired olefins, which results in a strongly adsorbed aromatic molecule. The formation of aromatic coke proceeds mostly by hydride transfer between olefins and carbon growth via multiple methylations of such aromatic species [83].

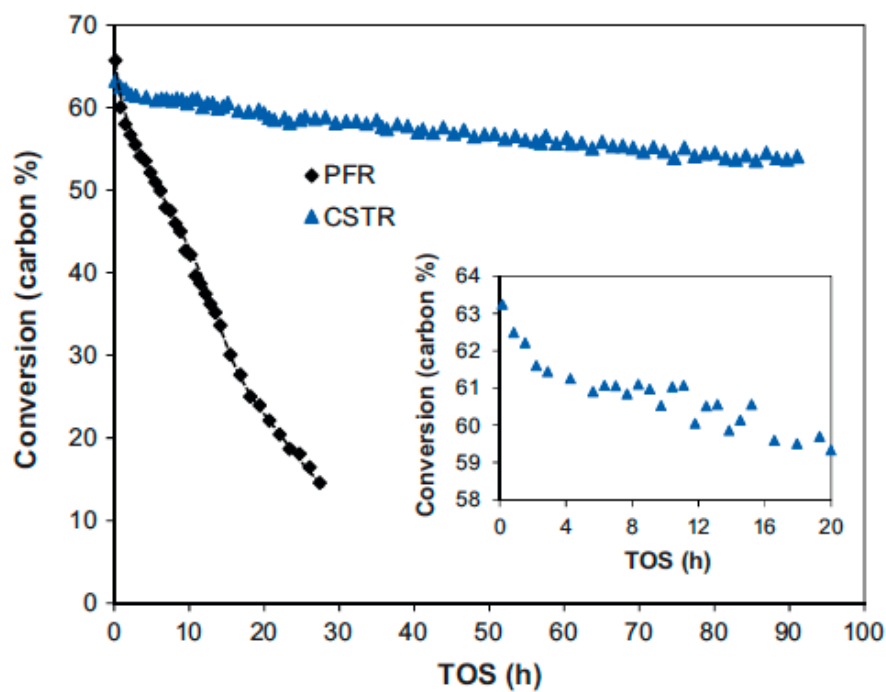


Figure 5. MTO reaction over the H-ZSM-5-S catalyst in the PFR at ambient pressure and the H-ZSM-5-S catalyst in the CSTR at 6.5 bar, $T = 723$ K and $p_{\text{MeOH}} = 178$ mbar. Adapted with permission from ref. [83]. Copyright 2015 Elsevier.

Zeolite-based catalysts that show promise for high olefin selectivity are unfortunately typically limited by mass transfer, suffering from rapid deactivation due to carbon deposition and water poisoning [83]. The issues with coke deactivation on the zeolite catalysts involved in MTO reactions are seen in classical MTO chemistry. The directed transformation of coke into active intermediates in a methanol-to-olefins catalyst was reported to boost the light olefin selectivity [84]. Another strategy to mitigate the deactivation was to synthesize nanozeolites, which have shortened diffusion paths, or mesoporous hierarchical zeolites, which exhibit longer catalyst lifetimes because of their larger pores and improved mass transfer [85–87].

With an Fe catalyst, the deactivation by coke is not related to the constriction of narrow pores, but several authors have reported the formation of carbonaceous residues on the active sites. Lee et al. investigated the deactivation behavior of an Fe-K/-Al₂O₃ catalyst, and found that the deactivation pathway was different according to the reaction position and reaction time. The main deactivation reason was the phase transformation at the top of the reactor. Conversely, the main factor at the bottom of the reactor was the deposited coke generated by secondary reactions. In particular, the produced olefins may have been adsorbed on acidic sites, and thus the olefins served as major precursors to coke. The SEM micrographs of the used catalysts clearly showed that most of the surface was covered by deposited graphite and graphite clusters protruding on the surface, mixed with some fine filamentous carbon (Figure 6) [57].

With these multiple deactivation pathways having been identified, it now becomes a critical issue to find ways of modifying the catalyst to become more stable. In the section directly below, we will describe the approaches that multiple researchers have examined in an attempt to mitigate deactivation.

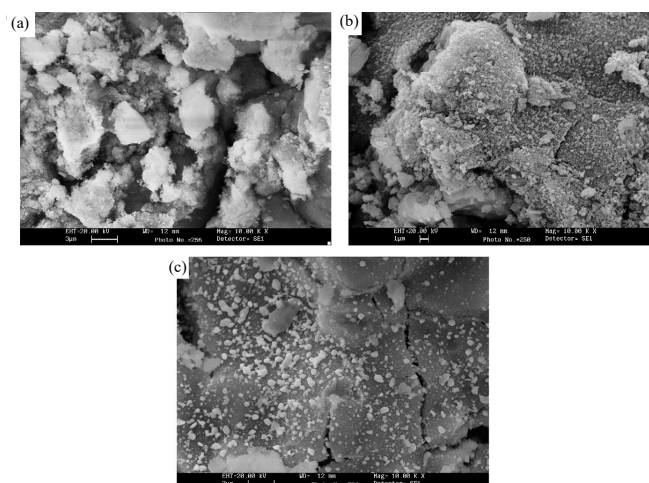


Figure 6. SEM image of the Fe-K/ γ -Al₂O₃ catalysts after the CO₂ hydrogenation reaction: (a) 100 h, (b) 300 h, and (c) 500 h. Adapted with permission from ref. [57]. Copyright 2009 Elsevier.

3. Recent Progress on the Mitigation of the Catalyst Deactivation

We will discuss the effect of promoters, metal oxide support, bifunctional composition and structure on the catalyst design to minimize the catalyst deactivation. We will summarize reports published within the last five years showing that promoters, supports, and novel morphology designs have mitigated the deactivation effects.

3.1. Promoter Effect

Fe-based catalysts have been widely studied in CO₂ hydrogenation, and usually show unsatisfactory selectivity toward lower olefins. The addition of suitable promoters to increase the yield of light olefins and the stability of the catalysts by controlling the electronic and structural properties have been extensively studied. Alkali metals such as K and Na have been broadly used as promoters to control the electronic properties. Mn, Ce, Ca metals have been used as structural promoters. Transition metals such as Zn, Co, Cu, V, Zr, etc., have been used as both electronic and structural promoters. Some representative catalysts on the promoter effect for CO₂ hydrogenation to light olefins with improved catalyst stability are presented in Table 1.

Table 1. Some representative catalysts on promoter effect for CO₂ hydrogenation to light olefins.

Catalyst	CO ₂ Conv., %	Selectivity, %				Yield, % C ₂ -C ₄ ⁼	O/P Ratio	Stability	Ref.
		CO	CH ₄	C ₂ -C ₄	C ₂ -C ₄ ⁰				
10Mn-Fe ₃ O ₄	44.7	9.4	22.0	46.2	7.1	18.7	6.5	24 h	[88]
0.58% Zn-Fe-Co/K-Al ₂ O ₃	57.8	8.8	6.2	63.2	21.8	19.9	2.9	50 h	[89]
Na-Zn-Fe	38.0	15.0	13.0	42.0	4.9	16.0	8.5	100 h	[90]
Na-CoFe ₂ O ₄	41.8	10.0	~18.0	37.2	~7.0	15.5	~5.3	100 h	[91]
Fe-Co/K-Al ₂ O ₃	40.0	12.2	24.8	46.1	7.9	16.2	5.9	6 h	[33]
0.5%Na-Fe ₅ C ₂	35.3	13.2	31.8	57.0	10.1	20.1	5.7	10 h	[92]
Fe-Zn-2Na	43.0	15.7	22.8	54.1	7.4	23.2	7.3	10 h	[93]
Fe/C-KHCO ₃	33.0	20.8	12.7	59.8 ^a	27.3	9.0	2.2	100 h	[94]
5Mn-Na/Fe	38.6	11.7	11.8	30.2	4.0	11.7	11.0	10 h	[95]
FeNa(1.18)	40.5	13.5	15.8	46.6	7.5	15.7	6.2	60 h	[31]
Na/Fe-Zn	30.6	n/a	13.0	26.8	3.9	8.4	6.9	200 h	[96]
Fe/C-Bio	31.0	23.2	11.8	21.7	24.4	6.7	0.9	6 h	[97]
5%Na/Fe ₃ O ₄	36.8	~11.0	~5.0	64.3	~13.0	23.7	~4.9	10 h	[98]
Fe/C+K(0.75)	40.0	~16.0	~22.0	~39.0	~12.0	~15.6	~3.3	50 h	[99]
35Fe-7Zr-1Ce-K	57.3	3.05	20.6	55.6	7.9	31.8	7.1	84 h	[100]
Fe-Mn/K-Al ₂ O ₃	29.4	20.2	18.7	48.7	6.5	14.3	7.4	>6 h	[101]
Fe-Cu(0.17)/K(1.0)	29.3	17.0	7.0	63.8	12.2	19.1	5.2	50 h	[102]
Na-CoFe ₂ O ₄ /CNT	34.4	19.0	~5.0	38.8	18.0	13.3	12.9	>24 h	[103]
Fe-Co-K(0.3)/TiO ₂	21.2	54.0	9.0	37.0 ^b	n/a	n/a	4.1	18 h	[104]
Fe ₂ Zn ₁	35.0	~15.0	~20.0	57.8 ^c	7.2	20.2	8.0	200 h	[28]
ZnCo _{0.5} Fe _{1.5} O ₄	49.6	~7.5	~17.5	36.1	~10.0	17.9	~3.6	80 h	[105]

^a refers to high valued olefins (HVO); ^b includes C₂-C₄ and C₅₊ hydrocarbons; ^c refer to C₂-C₇⁼ olefins.

Adding alkali metals (i.e., Na, K) could increase the selectivity towards light olefins due to the enhanced CO₂ adsorption on the more electron-rich Fe phases and suppressed H₂ chemisorption, which inhibits olefin re-adsorption. Numpilai et al. reported on the effect of varying the content of the K promoter on the Fe-Co/K-Al₂O₃ catalysts via the CO₂-FTS reaction pathway. Unpromoted catalysts evidenced low-light olefin yields when compared to K-promoted ones with an ascending K/Fe ratio from 0 to 2.5. The maximum light olefin (C₂⁼–C₄⁼) distribution of 46.7% and O/P ratio of 7.6 were achieved over the catalyst promoted with a K/Fe atomic ratio of 2.5. The positive effect of K's addition is attributed to the strong interaction of H adsorbed with the catalyst surface caused by the electron donor from K to Fe species. This notion is also rationalized by the fact that the K promoter enhances the bond strength of absorbed CO₂ and H₂, retarding the hydrogenation of olefins to paraffins. In the same operating conditions, the catalyst promoted with a K/Fe atomic ratio of 0.5 provides the maximum light olefin (C₂⁼–C₄⁼) yield of 16.4%, which is significantly higher than that of 2.5 KFe catalysts (13.4%). This is explained by the K enriched surface of 2.5 KFe catalysts significantly reducing the BET surface area and generating a hydrogen-lean environment, ultimately lessening the catalytic activity [101].

A different promoter source plays an important role to affect catalytic CO₂ hydrogenation. Han et al. demonstrated that as the series of K-promoters changes from K₂CO₃, CH₃COOK, KHCO₃, and KOH, the electron transfer from potassium to iron species is facilitated, which forms a more active and distinct χ -Fe₅C₂-K₂CO₃ interface during CO₂ hydrogenation. This results in a higher selectivity to light olefins (75%) and a higher CO₂ conversion (32%). In contrast, the non-carbonaceous K-promoters do not facilitate iron species to form iron carbides, which causes an undesirable catalytic performance (Figure 7a). Additionally, the close proximity between carbonaceous K-promoters and Fe/C catalyst components produced high olefin yields and catalytic stability (Figure 7b) [94]. Guo et al. reported that K derived from biological rather than inorganic precursors showed a stronger migration ability during the CO₂ hydrogenation to light olefins. These surface-enriched K ions extracted from corncoobs could promote the carburization of iron species to form more Fe₅C₂, promoting both the reverse water-gas shift reaction and subsequent C–C coupling [97].

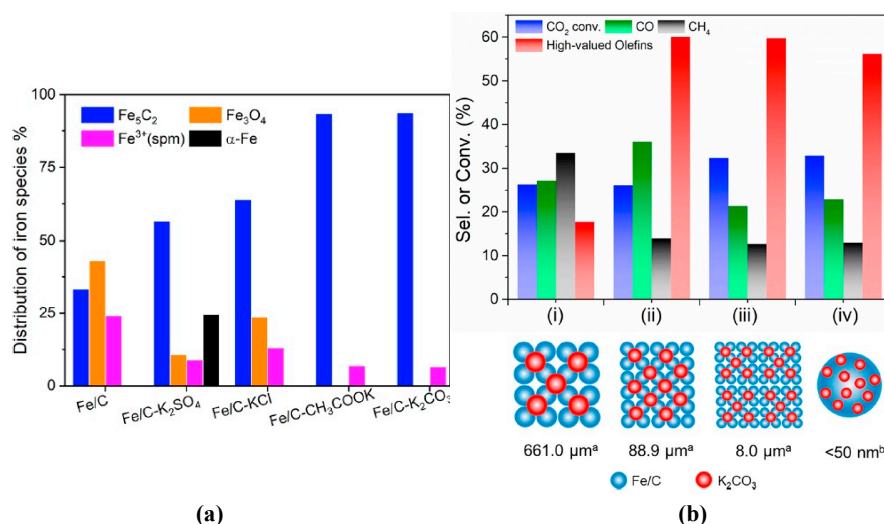


Figure 7. (a) Distribution of iron species content over different spent catalysts. (b) CO₂ hydrogenation over Fe/C–K₂CO₃ catalysts with varying proximity. Adapted with permission from ref. [94]. Copyright 2020 American Chemical Society.

Metal organic frameworks as precursors for the preparation of heterogeneous catalysts have been used recently [99,106,107]. Ramirez et al. used a metal organic framework as a catalyst precursor to synthesize a highly active, selective, and stable catalyst, as shown in Figure 8a–f for the hydrogenation of CO₂ to light olefins. Comparing the addition of Cu, Mo, Li, Na, K, Mg, Ca, Zn, Ni, Co, Mn, Fe, Pt, and Rh to an Fe/C composite, only K

is able to enhance olefin selectivity, as shown in Figure 8c. The presence of K promoted the formation of Fe_5C_2 and Fe_7C_3 carbides, as confirmed by XRD (Figure 8e). K helped keep a good balance between the iron oxide for RWGS and iron carbide for FTS. The results presented in Figure 8f indicated a trend in which methane formation decreased and olefin selectivity increased as the K loading increased. The catalyst $\text{Fe}/\text{C}+\text{K}(0.75)$ exhibited good stability (Figure 8d) and outstanding $\text{C}_2\text{--C}_4$ olefin space time yields of $33.6 \text{ mmol}\cdot\text{g}_{\text{cat}}^{-1}\cdot\text{h}^{-1}$ at $X_{\text{CO}_2} = 40\%$, 593K, 30 bar, $\text{H}_2/\text{CO}_2 = 3$, and $24,000 \text{ mL}\cdot\text{g}^{-1}\cdot\text{h}^{-1}$ [99].

Some work may shed light on the ways in which the alkali promoters affect the behavior of iron catalysts. By the precisely controlled addition of promoters to fine tune the catalytic performance for the hydrogenation of CO_2 to olefins, Yang et al. investigated how a zinc ferrite catalyst system could be affected by the addition of sodium and potassium promoters, specifically on the conversion of CO and CO_2 to olefins. It was found that the catalyst's composition of iron oxides and iron carbides was altered in the presence of the promoters, which affected the CO and CO_2 conversion. The production of C_{2+} olefins was greatly facilitated by the Na- and K-promoted catalysts. The Na/Fe-Zn catalyst was found to possess the optimal olefin productivity, and inhibited the competitive methanation reaction. It showed a total carbon conversion of 34.0%, which decreased by only 12.2% over 200 h [96]. Similarly, Wei et al. unraveled the effect of the Na promoter on the evolution of iron and carbon species, as well as the consequent tuning effect on the hydrogenation of CO_2 to olefins. With the contents of the Na promoter increasing from 0 wt% to 0.5 wt%, the ratio of olefins to paraffins (C_{2+}) rose markedly, from 0.70 to 5.67. The in situ XRD and temperature programmed surface reaction (TPSR) confirmed that the introduction of the Na promoter decreased the particle size of Fe_5C_2 and regulated the distribution of surface carbon species. Furthermore, the in situ XRD and Raman demonstrated that the interaction between the Na promoter and the catalysts inhibited the hydrogenation of Fe_5C_2 and surface graphitic carbon species, consequently improving the stability of the Fe_5C_2 and enhancing the formation of olefins by inhibiting the hydrogenation of the intermediate carbon species [92]. Using a similar approach, Liang et al. modified the xNa/Fe-based catalysts with tunable amounts of sodium promoter for CO_2 hydrogenation to alkenes, with CO_2 conversion at 36.8% and a light olefin selectivity of 64.3%. It was found that the addition of the Na promoter into Fe-based catalysts boosted the adsorption of CO_2 , facilitated the formation and stability of the active Fe_5C_2 phase, and inhibited the secondary hydrogenation of alkenes under the CO_2 hydrogenation reaction conditions (Figure 9a–c). The content of Fe_5C_2 correlated with the amount of Na is shown in Figure 9d [98].

Wei et al. synthesized a series of Fe_3O_4 -based nanocatalysts with varying sodium contents. The residual sodium markedly influenced the textural properties of the Fe_3O_4 -based catalysts, and faintly hampered the reduction of the catalysts. However, it discernibly promoted the surface basicity and prominently improved the carburization degrees of the iron catalysts, which is favored for olefin production. Compared with the sodium-free Fe_3O_4 catalysts, the sodium-promoted Fe_3O_4 catalysts displayed higher activity and selectivity for $\text{C}_2\text{--C}_4$ olefins. The FeNa catalyst (1.18) (Na/Fe weight ratio of 1.18/100) exhibited a high degree of catalytic activity with a high olefin/paraffin ratio (6.2) and selectivity to $\text{C}_2\text{--C}_4$ olefins (46.6%), and fairly low CO and CH_4 production at a CO_2 conversion of 40.5%. This catalyst also exhibited superb stability during the 100 h test at 593K. Comparing the scanning electron microscopy (SEM) image after reduction, there was no apparent indication of particle size growth after catalytic reaction for 100 h, further revealing the improved reaction stability of these iron nanoparticles [31]. Zhang et al. fabricated a Na- and Zn-promoted iron catalyst by a sol-gel method, and demonstrated its high activity, selectivity and stability towards the formation of C_{2+} olefins in the hydrogenation of CO_2 into C_{2+} olefins. The selectivity of the C_{2+} olefins reached 78%, and the space-time yield of olefins was as high as $3.4 \text{ g}\cdot\text{g}_{\text{cat}}^{-1}\cdot\text{h}^{-1}$. The catalyst was composed of ZnO and $\chi\text{-Fe}_5\text{C}_2$ phases with Na^+ dispersed on both ZnO and $\chi\text{-Fe}_5\text{C}_2$. Zhang et al. found that ZnO functions for the RWGS reaction of CO_2 to CO, while $\chi\text{-Fe}_5\text{C}_2$ is responsible for CO hydrogenation to olefins. The presence of Na^+ enhanced the selectivity of C_{2+} olefins by regulating the

hydrogenation ability and facilitating the desorption of olefins (Figure 10a). The presence of ZnO not only efficiently catalyzes the RWGS reaction but also improves the activity and stability of CO₂ hydrogenation by controlling the size of χ -Fe₅C₂ (Figure 10c,d). It was further discovered that the close proximity between ZnO and χ -Fe₅C₂ is beneficial for the conversion of CO₂ to olefins (Figure 10b). The larger interface could facilitate the diffusion and transfer of intermediate CO from ZnO to χ -Fe₅C₂, favoring CO₂ adsorption and subsequent CO hydrogenation to C₂₊ olefins [90]. Malhi et al. also investigated the effect of Na and Zn on iron-based catalysts, and found that the modified Fe-based catalyst exhibited a good performance for CO₂ hydrogenation to olefins, with a CO₂ conversion of 43%, a selectivity of 54.1% to C₂₊ olefins, and a high olefins-to-paraffins ratio of 7.3 [93].

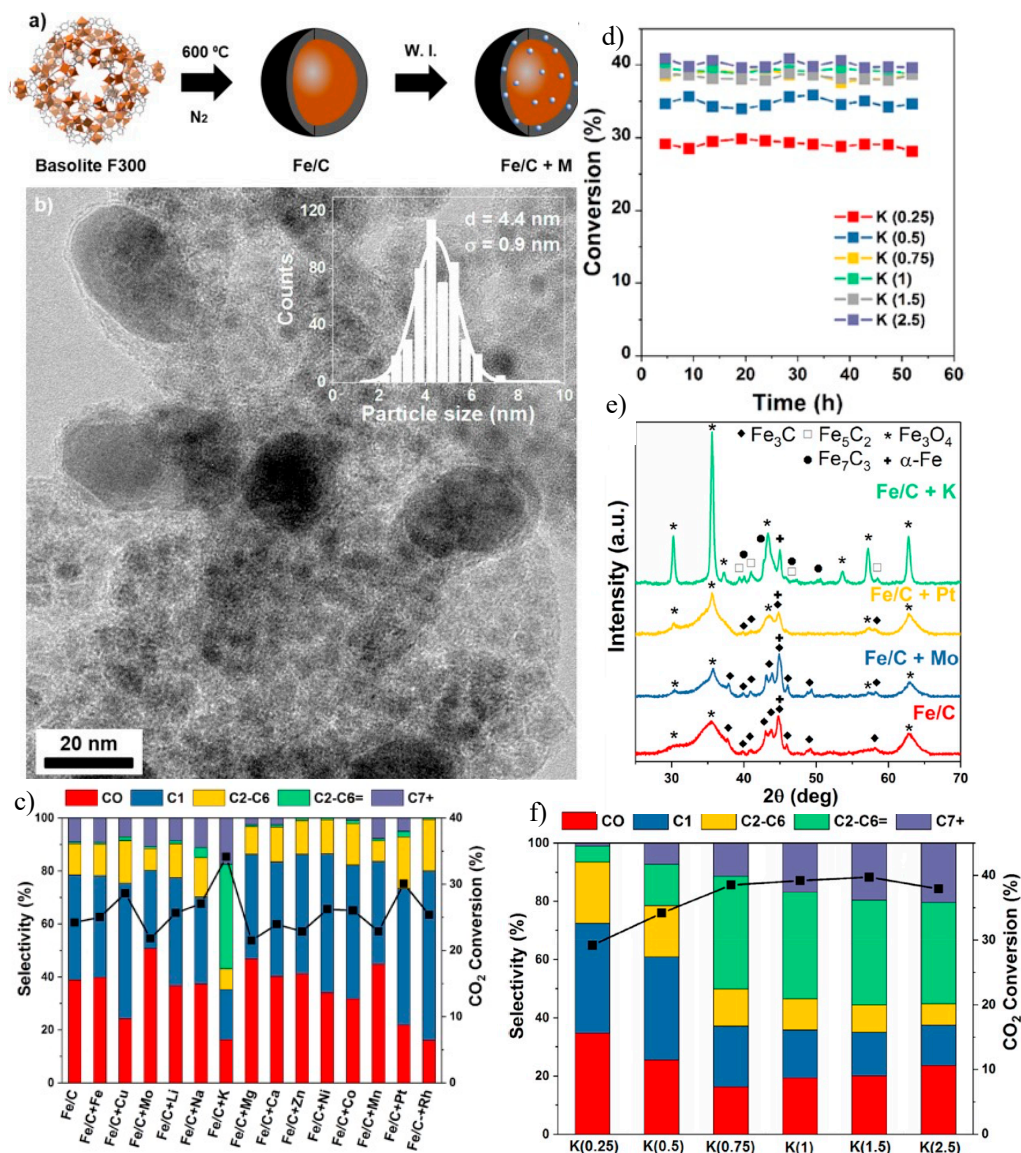


Figure 8. (a) Illustrated synthesis of Fe/C catalysts. (b) TEM image of Fe/C catalysts. (c) Catalytic performance over promoted and unpromoted Fe catalysts. (d) CO₂ conversion after 50 h of TOS. (e) XRD of promoted and unpromoted Fe catalysts. (f) Effect of K loading on the selectivity and CO₂ conversion after 50 h of TOS. Testing conditions: 593 K, 30 bar, H₂/CO₂ molar ratio = 3, and GHSV = 24,000 mL·g⁻¹·h⁻¹. Adapted with permission from ref. [99]. Copyright 2018 American Chemical Society.

Chaipraditgul et al. investigated the effect of transition metals (Cu, Co, Zn, Mn or V) on the Fe/K-Al₂O₃ catalyst and found that the inclusion of the transition metal remarkably affected the interaction between the catalysts' surface and the adsorptive CO₂ and H₂.

The Fe/K-Al₂O₃ promoted with Cu, Co or Zn showed a lower the olefin to paraffin ratio, owing to a markedly increased number of weakly adsorbed H atoms resulting from the enhanced hydrogenation ability of the promoted catalysts. On the contrary, the addition of a Mn promoter to Fe/K-Al₂O₃ reduced the number of weakly adsorbed H atoms, lowering the hydrogenation ability to result in a high olefin to paraffin ratio of 7.4. The presence of either Mn or V inhibited the CO hydrogenation to hydrocarbon, leading to the low CO₂ conversion, while the CO₂ conversion was enhanced by incorporating either Co or Cu onto the Fe/K-Al₂O₃ catalyst [33]. Gong et al. investigated the promoting effect that Cu had on Fe-Mn-based catalysts in the production of light olefins via the CO₂-FTS process. The Cu promoter was found to facilitate the reduction process and enhance CO dissociative adsorption by altering the interactions between Fe, Mn and the SiO₂ binder, which led to increased activity. The addition of Cu weakened the surface basicity, which in turn decreased the chain growth probability and yielded a higher selectivity of light olefins [108].

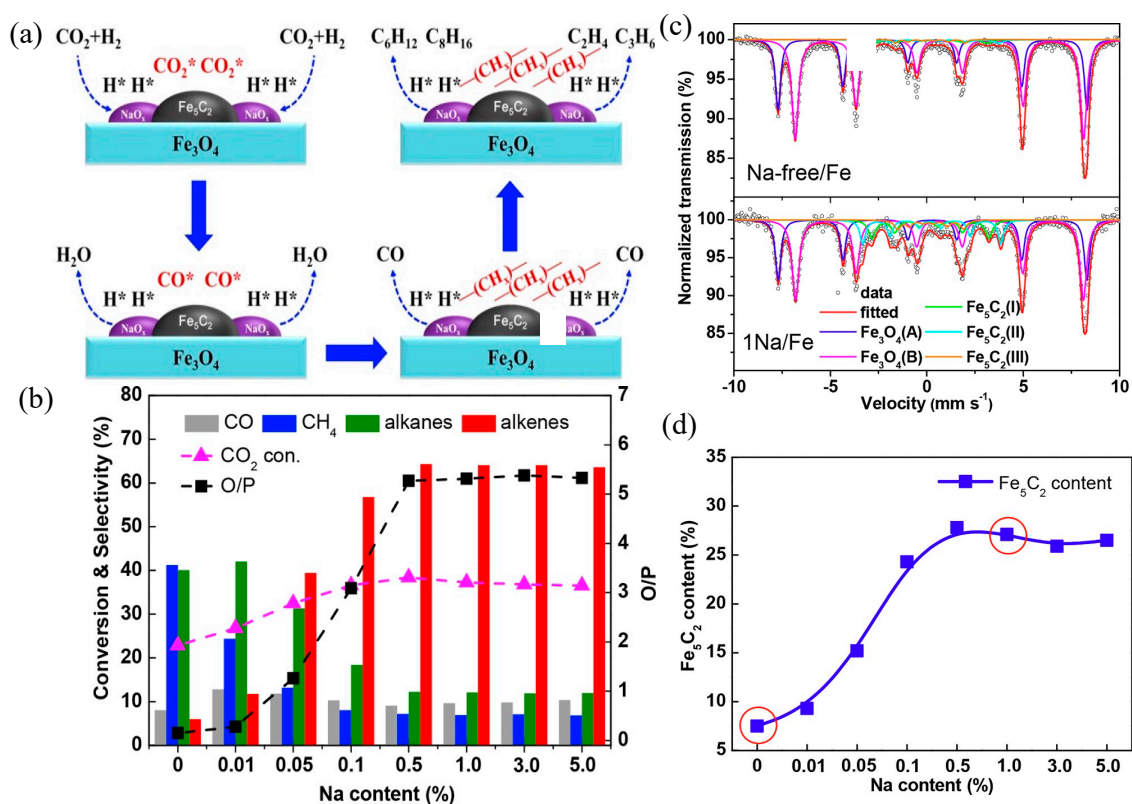


Figure 9. (a) Illustrated scheme of CO₂ hydrogenation. (b) Conversion and selectivity of CO₂ hydrogenation over an xNa/Fe catalyst (testing conditions: H₂/CO₂ molar ratio = 3; P = 3 MPa; T = 593 K; GHSV = 2040 mL h⁻¹ g_{cat}⁻¹; TOS = 10 h). (c) Mössbauer spectra of the spent Na-free/Fe and 1Na/Fe catalysts. (d) Fe₅C₂ content of the spent xNa/Fe catalyst vs. the Na content. Adapted with permission from ref. [98]. Copyright 2019 American Chemical Society.

Jiang et al. reported the synthesis of Mn-modified Fe₃O₄ microsphere catalysts. These catalysts demonstrated excellent catalytic performance, with a 44.7% CO₂ conversion, 46.2% light olefin selectivity, and 18.7% light olefin yield over the 10 Mn-Fe₃O₄ catalyst. The O/P ratio increased from 3.7 for the unpromoted Fe₃O₄ catalyst to 6.5 for the Mn-promoted catalyst. An even distribution of manganese was found over the surface of the Fe₃O₄ microsphere. Such homogeneous dispersion allows for an increase in the basicity of the catalyst, which prevents the further hydrogenation of olefins into paraffins. It was noted that the synergistic effects between Fe and Mn improve the dissociation and conversion of CO₂ to hydrocarbons. The addition of Mn was found to promote the production of Fe carbides and enhance the active phases of CO₂ hydrogenation and the FTS reaction, as well as preventing the hydrogenation of light olefins into paraffins and chain growth into

longer hydrocarbons [88]. A similar effect of the addition of Mn to Na/Fe catalysts was also observed by Liang et al. [95].

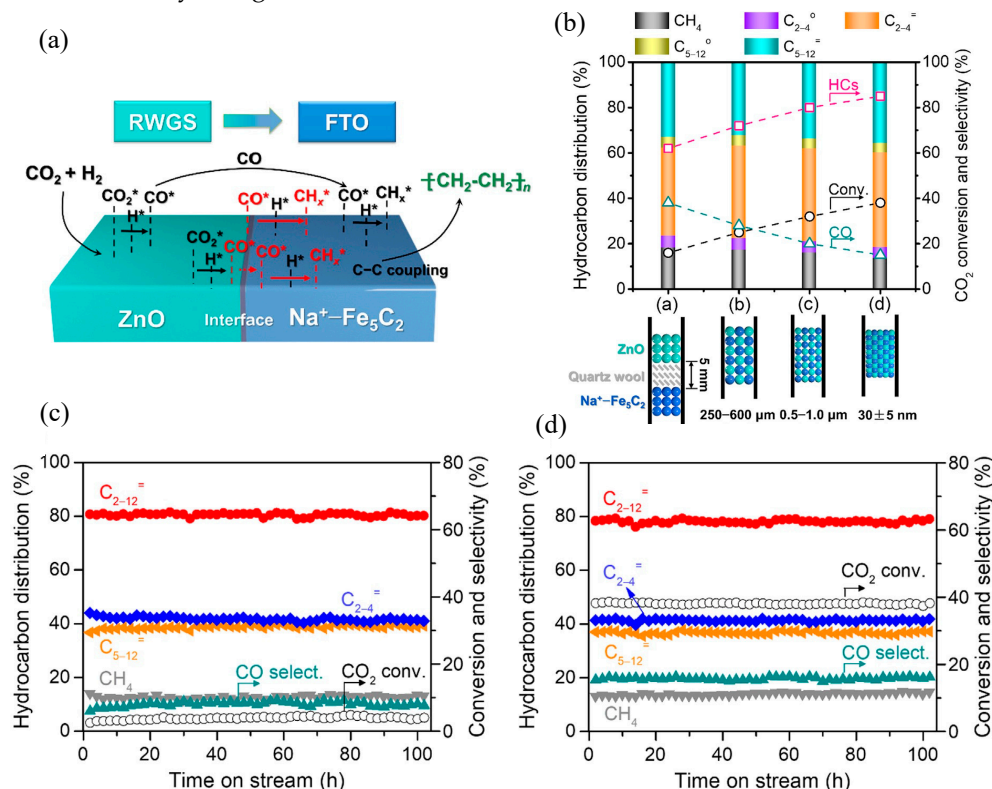


Figure 10. (a) Illustrated reaction mechanism for CO₂ hydrogenation over the catalyst Na-Zn-Fe. (b) Effect of the proximity between ZnO and Na⁺Fe₅C₂ on catalytic behaviors for CO₂ hydrogenation. Catalyst stability in CO₂ hydrogenation over (c) an Na⁺Fe₅C₂ catalyst and (d) a Na-Zn-Fe catalyst. Testing conditions: H₂/CO₂ molar ratio = 3, P = 2.5 MPa, W = 0.10 g, F = 25 mL min⁻¹, T = 613 K. Adapted with permission from ref. [90]. Copyright 2021 Elsevier.

Zhang et al. synthesized uniform microspheres of Fe-Zr-Ce-K catalysts by microwave-assisted homogeneous precipitation, and found that the reducibility, surface basicity and surface atom composition of the catalysts were greatly affected by varying the Ce content. CeO₂, as the structural promoter, restrained the growth of Fe₂O₃ crystallite, weakening the interaction between Fe species and zirconia, and enabling the easier reduction of Fe₂O₃. The best performance was obtained on a 35Fe-7Zr-1Ce-K catalyst at 593 K and 2 MPa, with a CO₂ conversion of 57.34%, a C₂–C₄ olefin selectivity of 55.67%, and a ratio of olefin/paraffin of 7 [100].

Extensive research efforts have been exerted on the development of bi-metallic catalysts for the conversion of CO₂ to light olefins. Yuan et al. demonstrated the influence of Na, Co and intimacy between Fe and Co on the catalytic performance of Fe-Co bimetallic catalysts for CO₂ hydrogenation that offers an olefin to paraffin ratio of 6 at a CO₂ conversion rate of 41%. With the introduction of Co into the Fe catalyst, the CO₂ conversion is significantly enhanced. The intimate contact between the Fe and Co sites favored the production of C₂–C₄⁼. When Na was added to the system, the surface of the catalyst became carbon-rich and hydrogen-poor, allowing C–C coupling to form light olefins and suppress the methane formation. Moreover, the addition of a Na promoter facilitated the generation of χ -(Fe_{1-x}Co_x)₅C₂ under the CO₂ hydrogenation reaction conditions, and thus further improved the catalytic performances. A superb stability over 100 h was observed (Figure 11) [91]. Witoon et al. investigated the effect of Zn addition to Fe-Co/K-Al₂O₃ catalysts. The addition of Zn resulted in the improved dispersion and reducibility of iron oxides. For example, the 0.58 wt% Zn-promoted Fe-Co/K-Al₂O₃ catalyst afforded a large number of active sites for the adsorption of CO and H₂ due to higher dispersion and an

eased reducibility (Figure 12a). The catalyst exhibited superior activity for light olefin formation with yield of 19.9% under the optimum testing conditions of 613 K, 25 bar, 9000 mL $g_{cat}^{-1} h^{-1}$ and a H_2/CO_2 ratio of 4. Figure 12b also shows a gradual decrease in the olefin to paraffin ratio, with an almost constant CO_2 conversion as a function of the time-on-stream (TOS). The X-ray photoelectron spectroscopy (XPS) analysis of the spent catalyst showed the continuous growth of iron carbide with the time-on-stream, indicating that iron carbide may be the active component resulting in paraffin production (Figure 12c). XRD confirmed the formation of Fe-C phases over the spent 0.58 wt% Zn-promoted Fe-Co/K- Al_2O_3 catalyst at the time-on-stream (Figure 12d) [89].

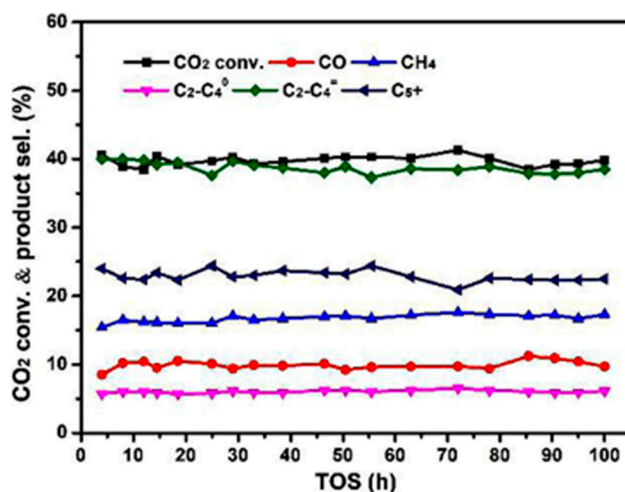


Figure 11. Catalytic performance of the CO_2 hydrogenation over the Na-CoFe₂O₄ catalyst at TOS (reaction conditions: H_2/CO_2 molar ratio = 3, $T = 593$ K, $P = 3$ MPa, $GHSV = 7200$ mL $h^{-1} g_{cat}^{-1}$, TOS = 100 h). Adapted with permission from ref. [91]. Copyright 2021 Elsevier.

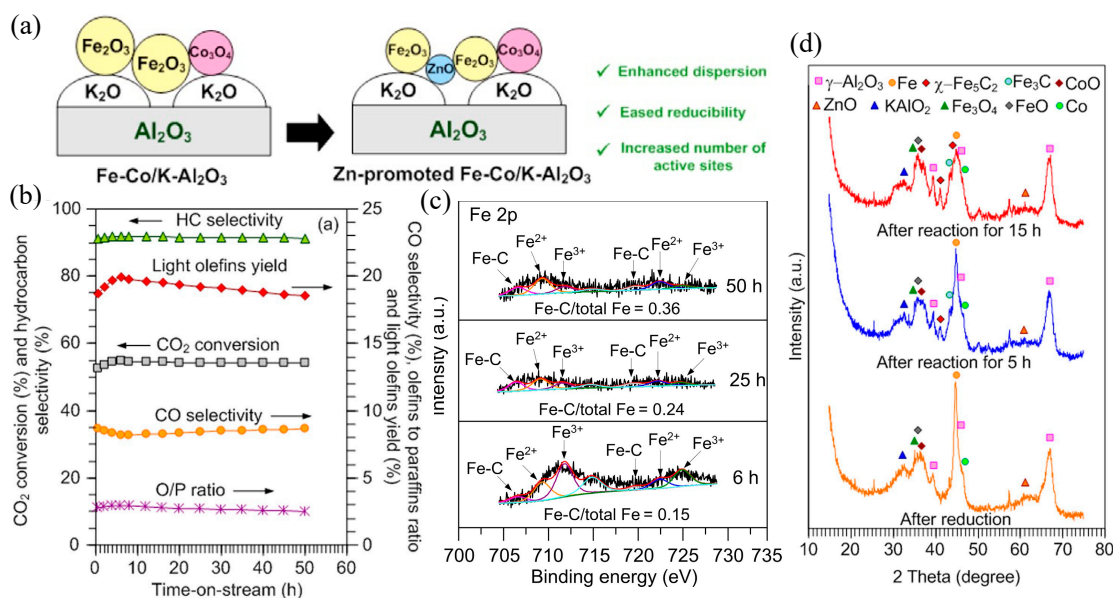
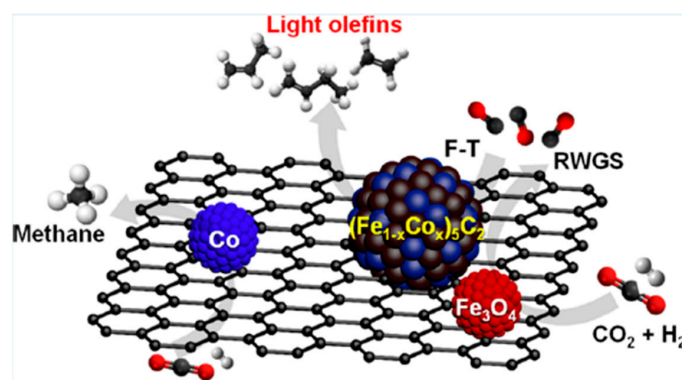


Figure 12. (a) Illustrated reaction mechanism. (b) Catalytic performance of the CO_2 hydrogenation over a Zn-promoted Fe-Co/K- Al_2O_3 catalyst. (c) XPS spectra (Fe 2p region) of the 0.58 wt% Zn-promoted Fe-Co/K- Al_2O_3 catalysts. (d) XRD pattern of the 0.58 wt% Zn-promoted Fe-Co/K- Al_2O_3 catalyst at varying TOS. Testing conditions: $T = 613$ K, $P = 25$ bar, $GHSV = 9000$ mL $g_{cat}^{-1} h^{-1}$ and H_2/CO_2 molar ratio = 4. Adapted with permission from ref. [89]. Copyright 2021 Elsevier.

Wang et al. reported the synthesis of γ -alumina supported Fe-Cu bimetallic catalysts, and found a strong bimetallic promotion for selective CO_2 conversion to olefin-rich C₂₊ hydrocarbons resulting from the combination of Fe and Cu at a specific composition. The suppression of the undesired CH₄ formation was achieved by the addition of Cu to Fe while

simultaneously enhancing the C–C coupling for C_{2+} hydrocarbon formation. The formation of the Fe–Cu alloy in the Fe–Cu(0.17)/ Al_2O_3 catalyst is suggested by the XRD results. Furthermore, the addition of K into the Fe–Cu considerably enhanced the production of C_2^- – C_4^- light olefins and the O/P ratio over Fe–Cu bimetallic catalysts. The Fe–Cu/K catalysts exhibited the superior selectivity of C_{2+} hydrocarbons compared to Fe–Co/K catalysts under the same reaction conditions [102]. Kim et al. synthesized monodisperse nanoparticles (NPs) of $CoFe_2O_4$ by the thermal decomposition of metal–oleate complexes, as shown in Scheme 4. The prepared NPs were supported on carbon nanotubes (CNTs), and Na was added to investigate the promoter and support effects on the catalyst for CO_2 hydrogenation to light olefins. The resulting Na– $CoFe_2O_4$ /CNT exhibited a superior CO_2 conversion of 34% and a light olefin selectivity of 39% compared to other reported Fe-based catalysts under similar reaction conditions. The superb performance of Na– $CoFe_2O_4$ /CNT was attributed to the formation of a bimetallic alloy carbide, $(Fe_{1-x}Co_x)_5C_2$. Higher CO_2 conversion and better light olefin selectivity were found in comparison with conventional Fe-only catalysts which possess χ - Fe_5C_2 active sites and drastically improved the C_{2+} hydrocarbon formation in comparison with Co-only catalysts which contain Co_2C sites [103].



Scheme 4. Schematic demonstration of CO_2 hydrogenation over CNT supported bi-metallic catalyst $CoFe_2O_4$. Adapted with permission from ref. [103]. Copyright 2020 American Chemical Society.

Song et al. investigated titania-supported monometallic and bimetallic Fe-based catalysts for CO_2 conversion, and found that the mono-metallic catalyst (Fe-, Co-, Cu-) performed poorly for C–C coupling reactions. However, adding a small amount of a second metal (Co and Cu) to Fe revealed the synergetic promotion on the CO_2 conversion and the space–time yields (STY) of hydrocarbon products. The inclusion of K and La as promoters further improved the activity, giving a higher hydrocarbon selectivity and O/P ratio, indicating that the promoter facilitated the CO_2 activation and C–C couplings over bi-metallic catalysts [106]. Zhang et al. investigated Fe–Zn bimetallic catalysts for CO_2 hydrogenation to C_{2+} olefins. A high C_{2+} olefin selectivity of 57.8% after 200 h of time-on-stream at a CO_2 conversion of 35.0% was obtained over an Fe_2Zn_1 catalyst. In bimetallic Fe_5C_2 -ZnO catalysts, the ZnO plays a crucial role in improving the performance by altering the structure of the Fe components. Without ZnO, the chief deactivation mechanism was attributed to a phase transition from FeC_x to FeO_x over Fe_2O_3 . However, with the addition of Zn to Fe_2O_3 , the phase transformation and the carbon deposits over Fe_2Zn_1 were greatly diminished. Furthermore, the addition of Na inhibited the oxidation of χ - Fe_5C_2 active species for Fe–Zn bimetallic catalysts. During activation, both Zn and Na were shown to migrate onto the catalysts' surfaces. The oxidation of FeC_x by H_2O and CO_2 was shown to be diminished by the interaction between Zn and Na [28].

Xu et al. investigated the roles of Fe–Co interactions over ternary spinel-type $ZnCo_xFe_{2-x}O_4$ catalysts for CO_2 hydrogenation to produce light olefins. As shown in Figure 13, a high light olefin selectivity of 36.1%, a low CO selectivity of 5.8% at a high CO_2 conversion of 49.6%, and an excellent catalyst stability were obtained over the $ZnCo_{0.5}Fe_{1.5}O_4$ via the RWGS–FTS reaction pathway. It was shown that during the CO_2 hydrogenation over

ternary $\text{ZnCo}_{0.5}\text{Fe}_{1.5}\text{O}_4$ catalysts, the formation of electron-rich Fe^0 atoms in the CoFe alloy phase significantly boosted the generation of the active $\chi\text{-Fe}_5\text{C}_2$, Co_2C , and $\theta\text{-Fe}_3\text{C}$ phases, in which the $\chi\text{-Fe}_5\text{C}_2$ phase facilitated the C–C coupling, the Co_2C species suppressed the formation of CH_4 , and the formation of the $\theta\text{-Fe}_3\text{C}$ phase with lower hydrogenation activity inhibited the second hydrogenation of light olefins [105].

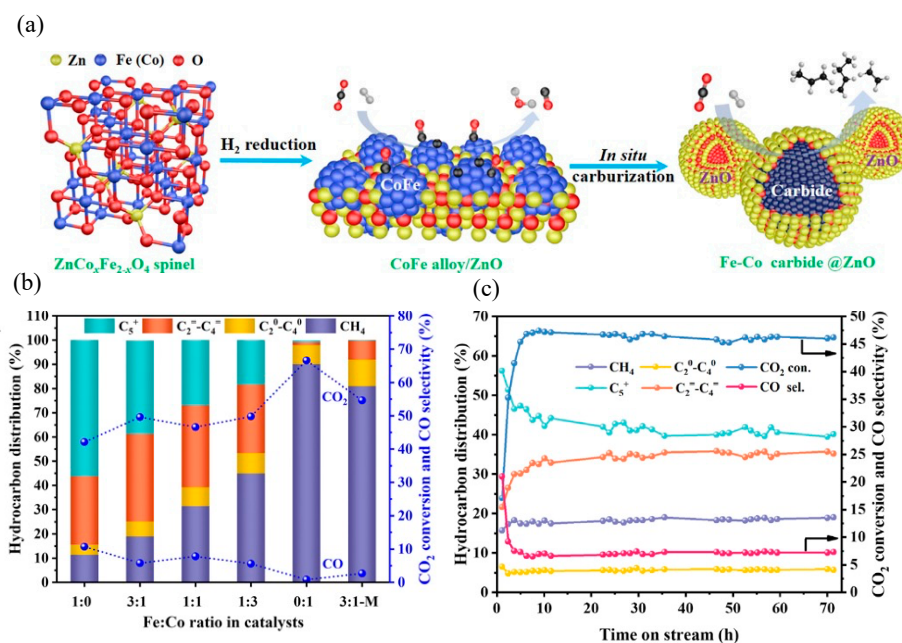


Figure 13. (a) Schematic illustration of the structural transformations of as-formed $\text{ZnCo}_x\text{Fe}_{2-x}\text{O}_4$ catalysts during the reduction and reaction steps. (b) CO_2 conversion and product distributions over K-containing $\text{ZnCo}_x\text{Fe}_{2-x}\text{O}_4$ catalysts with various Fe/Co molar ratios. (c) The stability of the K-containing $\text{ZnCo}_{0.5}\text{Fe}_{1.5}\text{O}_4$ catalyst in CO_2 hydrogenation (testing conditions: $T = 583\text{ K}$, $P = 2.5\text{ MPa}$, $\text{GHSV} = 4800\text{ mLh}^{-1}\text{g}_{\text{cat}}^{-1}$, CO_2/H_2 molar ratio = 1:3). Adapted with permission from ref. [105]. Copyright 2021 Elsevier.

In summary, the use of the appropriate K or Na promoter, the inclusion of Cu, Co, Zn, Mn or Ce in the Fe phase, and the bi-metallic formation played important roles for enhanced catalytic performance and stability.

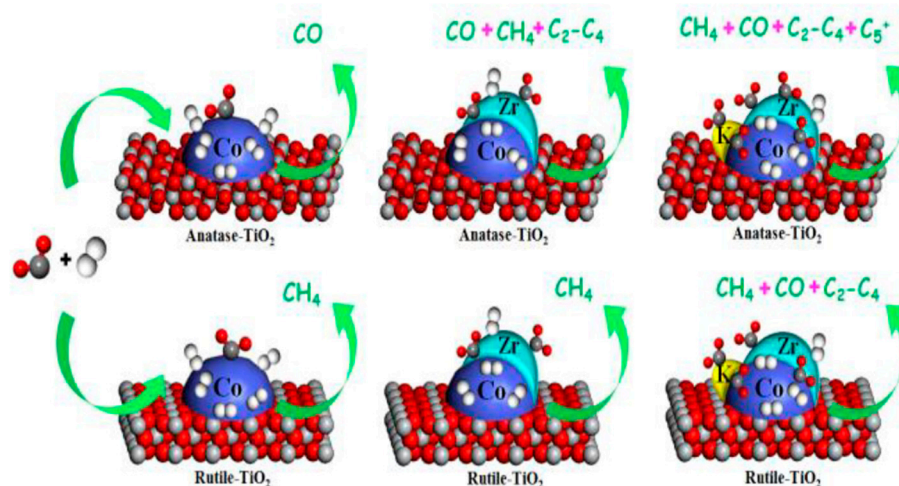
3.2. Support Effect

Catalyst support plays an important role in the overall activity and selectivity due to the interactions between the active metal components and the support during $\text{CO}_2\text{-FTS}$. Some representative catalysts of the support effect for CO_2 hydrogenation to light olefins with improved catalyst stability are presented in Table 2.

Table 2. Some representative catalysts of the support effect for CO_2 hydrogenation to light olefins.

Catalyst	CO_2 Conv., %	Selectivity, %				Yield, % $\text{C}_2\text{-C}_4^0$	O/P Ratio	Stability	Ref.
		CO	CH_4	$\text{C}_2\text{-C}_4^=$	$\text{C}_2\text{-C}_4^0$				
Fe-K/HPCMs-1	33.4	38.9	13.5	18.0	11.5	6.0	1.6	35 h	[109]
ZIF-8(a)/ Fe_2O_3	~24.0	~24.0	~21.0	~20.0	~24.0	~4.8	0.83	n/a	[110]
Fe(0.5)- Mo_2C^C	9.8	0.5	2.1	92.0	3.5	9.0	26.3	2 h	[111]
K-Zr-Co/a TiO_2	70.0	n/a	n/a	17.0	n/a	11.9	n/a	8h	[10]
Fe-Cr-K/ Nb_2O_5	31.0	57.0	32.0	10.0	1.0	3.1	3.1	n/a	[4]
15Fe-K/m- ZrO_2	38.8	19.9	30.1	42.8	12.8	16.6	3.3	12 h	[112]
20%Fe/Ce O_2 -NC	18.9	73.5	75.5	18.2	4.0	3.4	4.1	n/a	[113]
10Fe-1K/m- ZrO_2	40.5	n/a	n/a	15.0	n/a	6.1	n/a	100 h	[114]
Fe_5C_2 -10K/a- Al_2O_3	40.9	n/a	n/a	73.5	n/a	30.1	n/a	100 h	[15]
Co-Na-Mo/Ce O_2	15.1	70.2	22.1	10.7	36.0	1.6	0.03	n/a	[115]

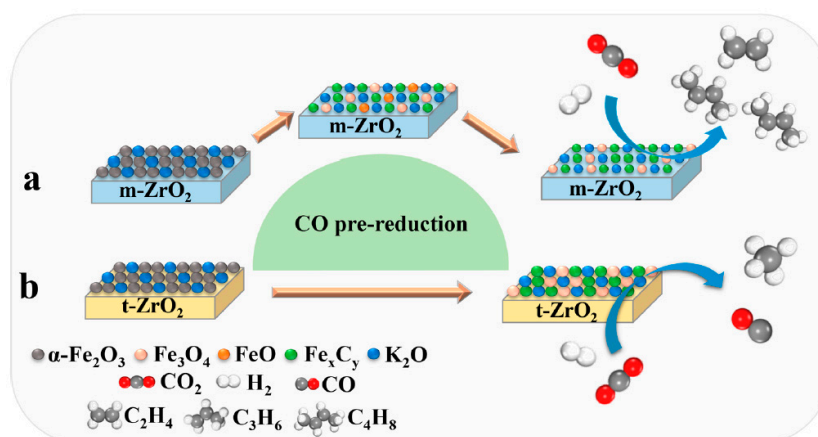
Owen et al. investigated the effect of Co-Na-Mo on various supports (SiO_2 , CeO_2 , ZrO_2 , $\gamma\text{-Al}_2\text{O}_3$, TiO_2 , ZSM-5 (NH_4^+) and MgO) for CO_2 hydrogenation. It was found that the surface area of the support and the metal–support interaction played a key role in the determination of the cobalt crystallite size, which strongly affected the catalytic activity. Cobalt particles with sizes < 2 nm supported on MgO showed low RWGS conversion with negligible FT activity, which is in agreement with the work of de Jong et al. [51]. When the cobalt particle size increased to 15 nm supported on SiO_2 and ZSM-5, both the CO_2 conversion and C_{2+} hydrocarbon selectivity increased markedly. When the cobalt particle size further increased to 25–30 nm, a lower CO_2 conversion but higher C_{2+} light olefin selectivity was obtained. The authors reported that the higher the metal–support interaction, the higher the growth chain probability of the hydrocarbons. By altering the $\text{TiO}_2/\text{SiO}_2$ ratio in the support, the CO_2 conversion and C_{2+} light olefin selectivity could be tuned [115]. Li et al. evaluated cobalt catalysts supported on TiO_2 with different crystal forms of anatase (a- TiO_2) and rutile (r- TiO_2), and it was found that the addition of Zr, K, and Cs improved the CO , CO_2 , and H_2 adsorption in both the capacity and strength over a- TiO_2 - and r- TiO_2 -supported catalysts. The surface C/H ratio increased drastically in the presence of promoters, leading to a high C_{2+} selectivity of 17% with 70% CO_2 conversion over a K-Zr-Co/a- TiO_2 catalyst. As a result, the product distribution could be tuned by adjusting the metal–support interaction and surface C/H ratio through Zr, K, and Cs modification over Co-based catalysts for CO_2 hydrogenation, as shown in Scheme 5 [10].



Scheme 5. Schematic illustration of CO_2 hydrogenation over unpromoted and Zr- and K-promoted cobalt catalysts supported on a- TiO_2 and r- TiO_2 . Adapted with permission from ref. [10]. Copyright 2013 American Chemical Society.

Da Silva et al. found the Fe-Cr catalyst, promoted with K and supported on niobium oxide, was more active (CO_2 conversion = 20%) and selective to light olefins (25%) compared to the same composition supported on silica (CO_2 conversion = 11%, light olefin selectivity = 18%) under the same testing conditions. Alkali metal promotion increased the selectivity of olefins, probably due to electron-donor effects and the basicity of niobium oxide. A niobium oxide-supported Fe-Cr catalyst presented higher activity and selectivity to olefins, which is probably due to strong metal–support interactions when compared with traditional SiO_2 [4]. Very recently, Huang et al. revealed the dynamic evolution of the active Fe and carbon species over different phases of zirconia (m- ZrO_2 and t- ZrO_2) on CO_2 hydrogenation to light olefins, as shown in Scheme 6. Fe-K/m- ZrO_2 catalysts performed better than the corresponding Fe-K/t- ZrO_2 catalysts under the optimal reaction conditions. Among them, the 15Fe-K/m- ZrO_2 catalyst showed remarkable catalytic activity, with a CO_2 conversion of 38.8% and a $\text{C}_2\text{-C}_4$ selectivity of 42.8%. More active species (Fe_3O_4 and $\chi\text{-Fe}_5\text{C}_2$) with smaller particle sizes were obtained for the Fe-K/m- ZrO_2 catalysts. The larger specific surface area facilitated the highly dispersed Fe species on the surface of the m- ZrO_2 support when compared to the t- ZrO_2 support. In addition, the

monoclinic phase $m\text{-ZrO}_2$ support provided more strong basic sites, effectively decreasing the deposited carbon species and coke generation. Moreover, the electron-donating ability of iron elements and more oxygen vacancies (Ov) improved the charge transfer between ZrO_2 and Fe. The synergy effect between K_2O and ZrO_2 fostered the generation of active carbide species. The formation of more $\chi\text{-Fe}_5\text{C}_2$ species contributed to the high yield of light olefins [112]. Similarly, Gu et al. investigated Fe-K supported on ZrO_2 with different crystal phases, revealing 40.5% CO_2 conversion, 15.0% light olefin selectivity, and excellent stability (Figure 14) over $10\text{Fe-1K}/m\text{-ZrO}_2$ (10 wt% Fe and 1 wt% K) at 2.0 MPa and 613 K. The CO_2 conversion was almost 200% higher than that of $10\text{Fe-1K}/t\text{-ZrO}_2$ [114].



Scheme 6. CO pre-reduction and CO_2 hydrogenation process on (a) $m\text{-ZrO}_2$ - and (b) $t\text{-ZrO}_2$ -supported Fe-Zr catalysts. Adapted with permission from ref. [112]. Copyright 2021 American Chemical Society.

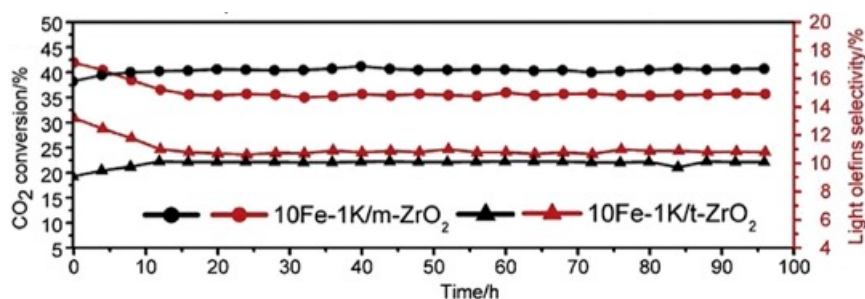


Figure 14. The stability of $10\text{Fe-1K}/m\text{-ZrO}_2$ and $10\text{Fe-1K}/t\text{-ZrO}_2$ for CO_2 conversion, and the light olefin selectivity at a TOS of 100 h at 613K. Adapted with permission from ref. [114]. Copyright 2019 Elsevier.

Torrente-Murciano demonstrated that iron-based catalysts could be improved not only through the inclusion of promoters but also by the judicious control of the morphology of the ceria support (nanoparticle, nanorods, nanocubes) for CO_2 hydrogenation to light olefins. For example, 20 wt% Fe/CeO_2 cubes provided better catalytic performance (CO_2 conversion = 15.2%, $\text{C}_2\text{-C}_4$ selectivity = 20.2%) when compared with nanorods and their nanoparticle counterparts. TPR showed that the ceria reducibility decreased in the order of rods > particles > cubes, suggesting that the catalytic effect had a direct dependence on the reducibility of the different nanostructured ceria supports and their interaction with the iron particles [113]. By the physical mixing of Fe_5C_2 and K-modified Al_2O_3 , Liu et al. discovered that $\text{Fe}_5\text{C}_2\text{-10K}/\alpha\text{-Al}_2\text{O}_3$ exhibited a CO_2 conversion of 40.9% and C_2+ selectivity of 73.5%, containing 37.3% $\text{C}_2\text{-C}_4$ and 31.1% C_5+ (Figure 15). The superior catalytic performance was due to the potassium which migrated into the Fe_5C_2 during the reaction, and the intimate contact between the Fe_5C_2 and $\text{K}/\alpha\text{-Al}_2\text{O}_3$. Among the various supports tested, as shown in Figure 15, alkaline Al_2O_3 is the best support for the high selectivity of value-added hydrocarbons [15].

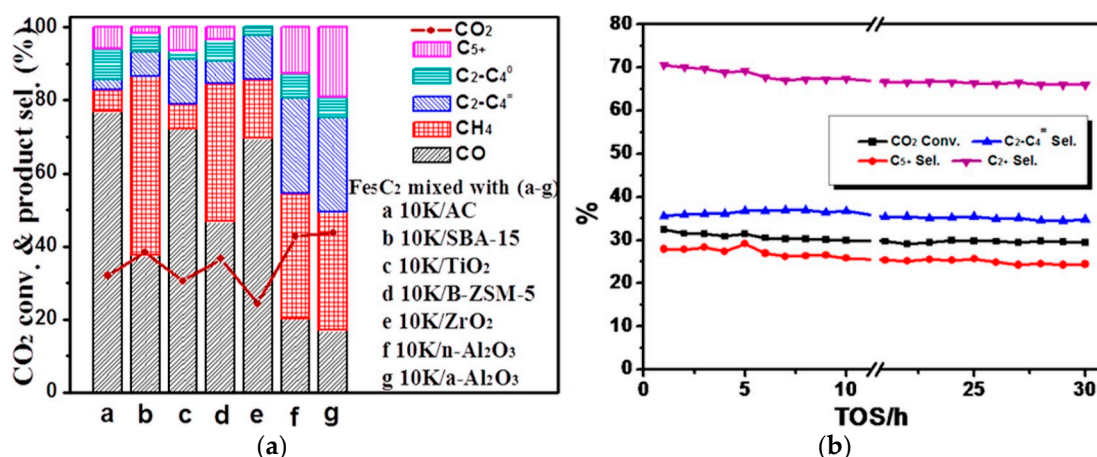


Figure 15. (a) Catalytic performance of CO_2 hydrogenation over Fe_5C_2 -based catalysts on various supports. (b) Catalytic performance and stability over an Fe_5C_2 -10K/a- Al_2O_3 catalyst (testing conditions: $T = 593\text{ K}$, $P = 3.0\text{ MPa}$, $\text{GHSV} = 3600\text{ mLg}^{-1}\text{h}^{-1}$, H_2/CO_2 molar ratio = 3). Adapted with permission from ref. [15]. Copyright 2018 American Chemical Society.

Dai et al. synthesized hierarchical porous carbon monoliths (HPCMs) by an adaptable strategy employing a one-step desilication process for a coke-deposited spent zeolite catalyst. This hierarchical porous carbon was shown to be a better support for the reduction of the nanoparticle size and heightening the synergism of the Fe–K catalyst for CO_2 hydrogenation, with a CO_2 conversion of 33.4% and a C_2^- – C_4^- selectivity of 18.0% [109].

Metal organic frameworks (MOFs) as novel porous materials had a considerable effect on the activity and selectivity of Fe-based catalysts. Hu et al. synthesized a type of hydrothermally stable MOF, zeolitic imidazolate frameworks (ZIF-8) with different sizes and morphologies, which were used as supports for CO_2 hydrogenation. The acidity, internal diffusion process and crystal size enabled the ZIF-8 supports to show different levels of substantial light olefin selectivity [110]. Raghav et al. developed a simple method for the synthesis of hierarchical molybdenum carbide ($\beta\text{-Mo}_2\text{C}$). The $\beta\text{-Mo}_2\text{C}$ phase exhibited the strongest metallic and some ionic character, and it behaved as both a support and co-catalyst for CO_2 hydrogenation to light olefins. The $\text{Fe}(0.5)\text{-Mo}_2\text{C}$ catalyst exhibited a conversion of CO_2 of 7.3% and a C_2^- olefin selectivity of 79.4% at 300 °C and 4.0 mPa. The XRD patterns of the fresh and used $\text{Fe}(0.5)\text{-Mo}_2\text{C}$ catalyst did not show a noticeable difference, indicating the stability of the catalysts to achieve high olefin selectivity [111].

In summary, various supports (SiO_2 , CeO_2 , $m\text{-ZrO}_2$, $\gamma\text{-Al}_2\text{O}_3$, TiO_2 , ZSM-5, MgO, NbO HPCMs, MOFs, $\beta\text{-Mo}_2\text{C}$) have been used for the dispersal of active species. The surface area, basicity, reducibility, oxygen vacancies, and morphology of the support played important roles, in most cases with the presence of promoters (K, Zr, Cs), in affecting the amount and particle size of the active carbide species; the synergy effect; the metal–support interaction; the strength and capacity of the CO, CO_2 , and H_2 adsorption on support; and the surface C/H ratio for CO_2 hydrogenation. By tuning the above-mentioned characteristics properly, the physically deposited carbon species, coke generation and metal sintering could be mitigated as reported.

3.3. Bifunctional Composite Catalyst Effect

The zeolite–methanol composite catalyst can also be improved by compositional modifications. The composite catalyst is composed of two functional components: one is the target for methanol synthesis, mainly Cu, Zn, and In metal oxide catalysts; the other one is for the MTO process, mainly zeolite catalysts. Here, in this section, the recent progress on composite catalysts for improved catalytic performance and stability are described accordingly. Some representative catalysts for the bifunctional composite catalyst effect

for CO₂ hydrogenation to light olefins with improved catalyst stability are presented in Table 3.

Table 3. Some representative catalysts for the bifunctional composite catalyst effect for CO₂ hydrogenation to light olefins.

Catalyst	CO ₂ Conv., %	Selectivity, %				Yield, % C ₂ –C ₄ ^o	O/P Ratio	Stability	Ref.
		CO	CH ₄	C ₂ –C ₄ ⁼	C ₂ –C ₄ ^o				
CuO-ZnO & SAPO-34	41.3	9.3	11.8	63.4	15.5	26.2	4.1	13 h	[116]
(CuO-ZnO)-kaolin & SAPO-34	57.6	9.6	11.4	63.8	15.2	36.7	4.2	20 h	[116]
In ₂ O ₃ /ZrO ₂ & SAPO	19.0	87.0	~17.0	90.0 ^a	n/a	17.1	n/a	>50 h	[43]
In ₂ O ₃ /ZrO ₂ & SAPO	~14.0	<5.0	<5.0	70.0	n/a	9.8	n/a	>100 h	[44]
In–Zr/SAPO-34	26.7	n/a	4.3	76.4 ^a	~14.0 ^a	20.4	5.5	>150 h	[19]
Zn _{0.5} Ce _{0.2} Zr _{1.8} O ₄ & H-RUB-13 (200)	10.7	28.3	2.9	83.4	5.4	8.9	15.4	>30 h	[117]
ZnZrO _x & bio-ZSM-Si	10.0	~80.0	5.5	64.4	30.1	6.4	2.1	60 h	[118]
InCrO _x (0.13) & SAPO	33.6	55.0	35.0	75.0 ^a	20.0 ^a	11.3	3.8	>120 h	[119]
ZnZrO & SAPO-34	12.6	47.0	3.0	80.0 ^a	14.0 ^a	10.1	5.7	>100 h	[14]
CZZ@Zn & SAPO-34	~7.0	n/a	~18.0	72.0	8.0	1.3	8.6	>120 h	[120]
In ₂ O ₃ -ZnZrO _x & SAPO-34-S-a	17.0	55.8	1.6	85.0 ^a	11.1 ^a	14.5	7.7	>90 h	[42]
In ₂ O ₃ -ZnZrO _x & SAPO-34-H-a	17.0	53.4	1.2	84.5 ^a	11.0 ^a	14.4	7.7	>90 h	[42]
ZnAl ₂ O ₄ & SAPO-34	15.0	49.0	0.7	87.0 ^a	10.0 ^a	13.1	8.7	10 h	[121]
ZnGa ₂ O ₄ & SAPO-34	13.0	46.0	1.0	86.0 ^a	11.0 ^a	11.2	7.8	10 h	[121]
ZnO-ZrO ₂ & Mn _{0.1} SAPO-34	24.4	42.2	3.7	61.7	33.6	15.1	1.8	10 h	[122]
In-Zr (4:1) & SAPO-34	26.2	63.9	2.0	74.5 ^a	21.5 ^a	19.5	3.5	>140 h	[18]

^a CO is not considered when calculating selectivity.

Wang et al. prepared kaolin-supported CuO-ZnO/SAPO-34 catalysts using kaolin as the support and raw material to prepare SAPO-34 molecular sieves. It was found that the resultant SAPO-34 molecular sieves showed a lamellar structure, relatively high crystallinity, and a larger specific surface area, which enabled the good dispersion of CuO-ZnO on the surface of the kaolin, and exposed more active sites for CO₂ conversion. The confinement effect of (CuO-ZnO)-kaolin/SAPO-34 catalysts could prevent methanol dissipation, and provided an increased driving force for the conversion of CO₂. Furthermore, the lamellar structure of SAPO-34 molecular sieves shortened the diffusion path of the intermediate product, and therefore enhanced the catalytic lifetime [116].

Gao et al. shown a selective hydrogenation process to directly convert CO₂ to light olefins via a bifunctional catalyst composed of a methanol synthesis catalyst (In₂O₃-ZrO₂) and a MTO catalyst (SAPO-34) by simple physical mixing. This bifunctional process exhibited an outstanding light olefin (C₂–C₃⁼) selectivity of 80–90% with a CO₂ conversion of ~20% and superior catalyst stability, running 50 h without obvious deactivation. The excellent catalytic performance was ascribed to the hybrid catalyst that suppressed the usually uncontrollable surface polymerization of CH_x in conventional CO₂-FTS. This was the highest selectivity reported to date, which dramatically surpassed the value obtained from traditional Fe or Co CO₂-FTS catalysts (typically less than 50%) [43].

Similarly, Tan et al. evaluated CO₂ conversion to light olefins over an In₂O₃-ZrO₂/SAPO-34 hybrid catalyst. This hybrid catalyst combined a In₂O₃-ZrO₂ component, which would provide the benefit of oxygen vacancy to foster CO₂ activation for hydrogenation into methanol, and a SAPO-34 component, to provide sites for the dehydration of the formed methanol into light olefins (Figure 16a). The light olefin selectivity reached 77.6% with less than 5% CO formation, which was ascribed to the strong adsorption of CO₂ to defects in the In₂O₃ and ZrO₂ components, creating a large energy barrier that suppressed CO₂ dissociation into CO. The weaker acidity from In₂O₃-ZrO₂ suppressed the further hydrogenation of the generated light olefins to paraffins. The catalyst displayed excellent stability, running for 100 h without obvious deactivation (Figure 16b) [44].

Furthermore, Gao et al. discovered that a bifunctional catalyst with an appropriate proximity containing In–Zr oxide, which was responsible for the CO₂ activation, and SAPO-34, which was responsible for the selective C–C coupling, could greatly improve the CO₂ hydrogenation to lower olefins with excellent selectivity (80%) and high activity (35% CO₂ conversion) (Figure 17a). They showed that the incorporation of zirconium significantly improved the catalytic stability by preventing the sintering of the oxide

nanoparticles caused by the increase in surface oxygen vacancies. No obvious deactivation was observed over 150 h (Figure 17b) [19].

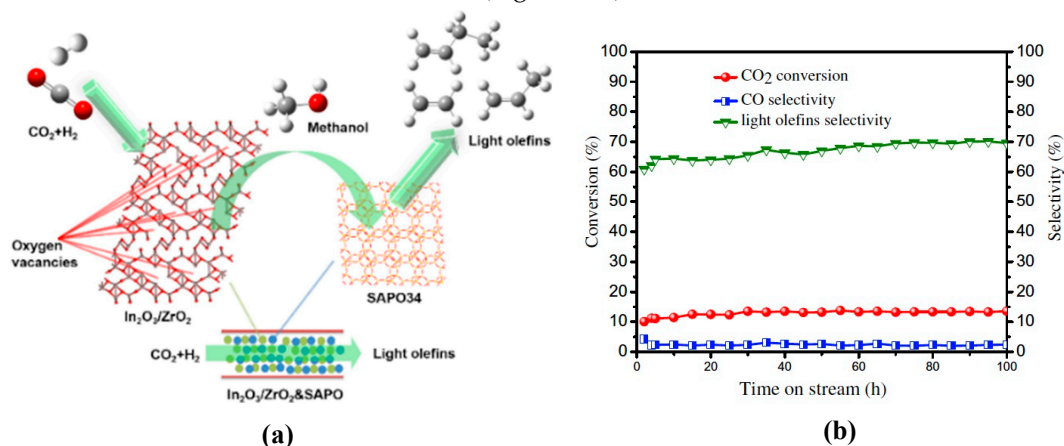


Figure 16. (a) Illustrated reaction mechanism over the bifunctional composite catalyst $\text{In}_2\text{O}_3\text{-ZrO}_2/\text{SAPO-34}$, and (b) the stability of the $\text{In}_2\text{O}_3\text{-ZrO}_2/\text{SAPO-34}$ composite catalyst for CO_2 hydrogenation to light olefins (testing conditions: $P = 2.0 \text{ MPa}$, $T = 573 \text{ K}$, $\text{GHSV} = 2160 \text{ cm}^3\text{h}^{-1}\text{g}_{\text{cat}}^{-1}$). Adapted with permission from ref. [44]. Copyright 2019 Elsevier.

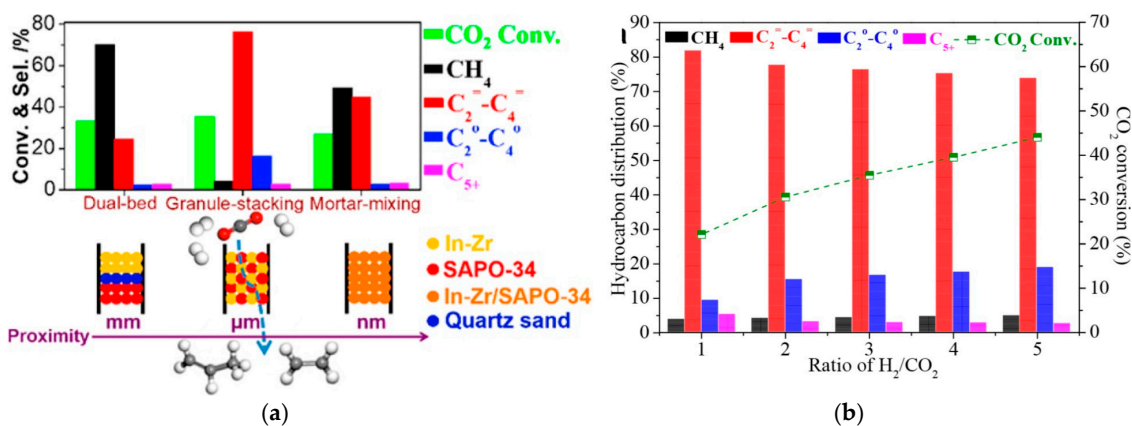


Figure 17. (a) Effect of the proximity of the active components on the CO_2 conversion and product selectivity, and (b) the catalytic stability of the composite catalyst In-Zr/SAPO-34 (testing conditions: $T = 673 \text{ K}$, $P = 3.0 \text{ MPa}$, $\text{GHSV} = 9000 \text{ mL g}_{\text{cat}}^{-1} \text{ h}^{-1}$, molar ratio of $\text{H}_2/\text{CO}_2/\text{N}_2 = 73/24/3$, and mass ratio of oxide/zeolite = 2). Adapted with permission from ref. [19]. Copyright 2018 American Chemical Society.

Wang et al. developed a new catalyst system composed of a $\text{Zn}_{0.5}\text{Ce}_{0.2}\text{Zr}_{1.8}\text{O}_4$ solid solution and H-RUB-13 zeolite. This composite exhibited a remarkable $\text{C}_2^- - \text{C}_4^-$ yield as high as 16.1%, with a CO selectivity of only 26.5% due to the hindering of the RWGS reaction. It was demonstrated that methanol was first generated on the $\text{Zn}_{0.5}\text{Ce}_{0.2}\text{Zr}_{1.8}\text{O}_4$ solid solution via the formate–methoxyl intermediate mechanism, and was then converted into light olefins on H-RUB-13. By adjusting the H-RUB-13 acidity, the light olefin distribution can be effectively regulated, with propene and butene accounting for 90% of the light olefins [117].

Li et al. proposed a new synthetic strategy to prepare the bifunctional catalysts $\text{ZnZrO}_x/\text{bio-ZSM-5}$. Hierarchically porous structured bio-ZSM-5 was prepared by using a natural rice husk as a template, which was then integrated with the ZnZrO_x solid solution nanoparticles by physical mixing. The derived bifunctional catalysts ZnZrO_x and bio-ZSM-5 exhibited superior light olefin selectivity and stability due to their unique pore structure, which was advantageous for mass transport and coke formation inhibition. $^*\text{CH}_x\text{O}$ was identified to be the key intermediate formed on the ZnZrO_x surface, and was transferred to the Brønsted acid sites in the bio-ZSM-5 for the subsequent conversion to light olefins. The addition of a Si promoter to the $\text{ZnZrO}_x/\text{bio-ZSM-5}$ catalyst prominently enhanced the

light olefin selectivity. The $\text{ZnZrO}_x/\text{bio-ZSM-5-Si}$ catalyst exhibited an outstanding light olefin selectivity of 64.4%, with a CO_2 conversion of 10% and an excellent stability without noticeable deactivation during 60 h on stream (Figure 18a). In addition, the proximity of the catalyst components plays a key role in light olefin selectivity. As seen in Figure 18b, increasing the proximity resulted in a greater olefin selectivity [118]. By incorporating proper amounts of Ce or Cr ions into indium oxides, the methanol selectivity is increased, along with a reduction in the CH_4 amount, as shown in Figure 19. Upon complexing with SAPO-34, a CO_2 conversion of 33.6% and a $\text{C}_2^+=\text{C}_4^+$ selectivity of 75.0% were achieved over $\text{InCrO}_x(0.13)/\text{SAPO-34}$, which was about 1.5–2.0 times those obtained on $\text{In}_2\text{O}_3/\text{SAPO-34}$ and $\text{In-Zr}/\text{SAPO-34}$. This is because the incorporation of Ce or Cr ions into In_2O_3 lattice sites promoted the generation of more surface oxygen vacancies, as shown in Figure 19a, and enhanced the electronic interaction of HCOO^* with $\text{InCeO}_x(0.13)$ and $\text{InCrO}_x(0.13)$ surfaces, which decreased the free energy barrier and enthalpy barrier for the formation of HCOO^* and CH_3OH . The composite catalysts also displayed excellent stability after 120 h on stream (Figure 19b) [119].

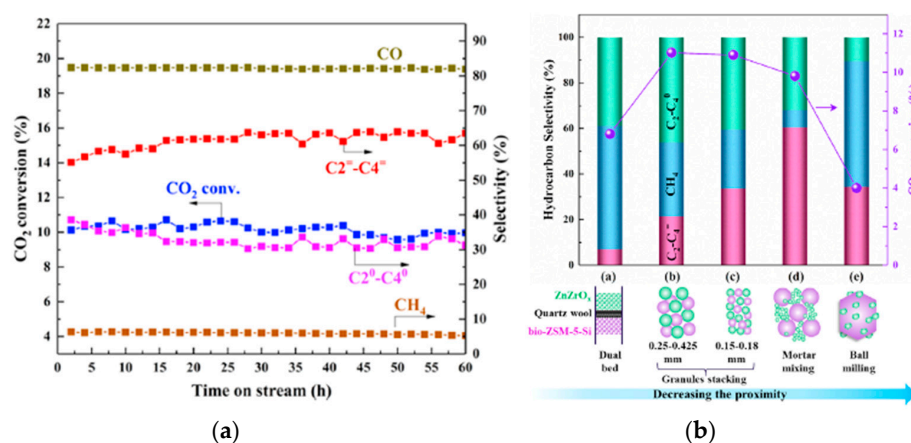


Figure 18. (a) Catalytic performance over the bifunctional composite catalysts $\text{ZnZrO}_x/\text{bio-ZSM-5-Si}$ at TOS (testing conditions: mass of catalyst = 0.6 g, $T = 653$ K, $P = 3$ MPa, gas flow rate = 20 mL min^{-1}). (b) Effect of the proximity of the active components of $\text{ZnZrO}_x/\text{bio-ZSM-5-Si}$ on the catalytic performance. Adapted with permission from ref. [118]. Copyright 2021 American Chemical Society.

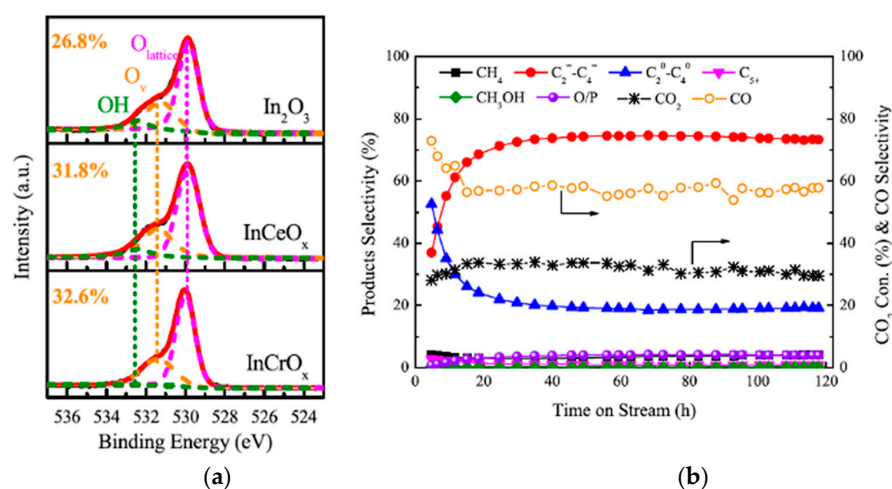


Figure 19. (a) The content of the surface oxygen vacancies (O_v) from O (1s) XPS spectra for the catalysts In_2O_3 , $\text{InCeO}_x(0.13)$, and $\text{InCrO}_x(0.13)$. (b) The catalytic stability of the bifunctional composite catalysts $\text{InCrO}_x(0.13)$ and SAPO-34 for CO_2 hydrogenation (testing conditions: H_2/CO_2 molar ratio = 3/1, $T = 623$ K, $P = 3.5$ MPa, and $\text{GHSV} = 1140 \text{ mL}_{\text{cat}}^{-1}\text{h}^{-1}$). Adapted with permission from ref. [119]. Copyright 2020 Elsevier.

Similarly, Li et al. developed a bifunctional composite catalyst ZnZrO/SAPO-34 containing a ZnOZrO₂ component to activate CO₂ and H₂ to form methanol, and a SAPO-34 component to perform C–C bond formation for the conversion of the produced methanol to light olefins. The derived dual function tandem catalyst exhibited an outstanding light olefin selectivity of 80% with good stability, and a CO₂ conversion of 12.6% (Figure 20a,b). The kinetic and thermodynamic coupling between the tandem reactions enabled the highly efficient conversion of CO₂ to lower olefins through the transfer and migration of CH_xO intermediate species [13].

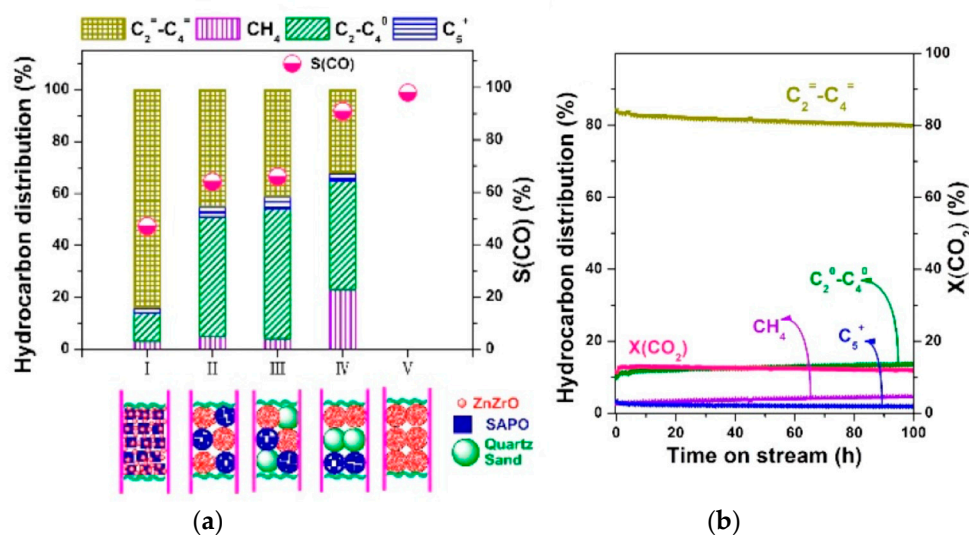


Figure 20. (a) CO₂ hydrogenation over the bifunctional composite catalyst ZnZrO/SAPO-34, with the effect of the proximity of the active components of ZnZrO and SAPO-34 on the catalytic performance. (b) The catalytic stability of the catalyst ZnZrO/SAPO-34 (testing conditions: T = 653K, P = 2 MPa, and GHSV = 3600 mL g_{cat}⁻¹ h⁻¹). Adapted with permission from ref. [13]. Copyright 2017 American Chemical Society.

Dang et al. advanced a series of dual function tandem catalysts containing In₂O₃-ZnZrO_x oxides and various SAPO-34 zeolites with varying crystal sizes (0.4–1.5 mm) and pore structures. It was found that decreasing the crystal size of SAPO-34 could shorten the diffusion path from the surface to the acid sites inside the zeolite pores, thus favoring the mass transfer of intermediate species for efficient C–C coupling to produce lower olefins and enhance the selectivity of C₂⁻-C₄⁼. Interestingly, further HNO₃ post-treatment caused the formation of the SAPO-34 zeolites with a hierarchical structure comprised of micro-/meso-/macropores, and reduced the amount of the Brønsted acid sites, both of which led to a significant increase in the catalytic performance, with the C₂⁻-C₄⁼ selectivity reaching as high as 85% among all of the hydrocarbons (Figure 21a), a very low CH₄ selectivity of only 1%, and an O/P ratio of 7.7 at a CO₂ conversion of 17%. The C₂⁻-C₄⁼ selectivity is much higher than the maximum predicted by the Anderson–Schulz–Flory distribution over modified FTS catalysts. The composite catalysts also exhibited excellent stability after 90 h on stream (Figure 21b) [42].

Liu et al. synthesized bifunctional composite catalysts composed of a spinel binary metal oxide ZnAl₂O₄/ZnGa₂O₄ and SAPO-34, with the selectivity of C₂-C₄ olefins reaching 87% at CO₂ conversions of 15%. This study revealed that the oxygen vacancy site on metal oxides played a crucial role in the adsorption and activation of CO₂, while the -Zn-O-domain accounted for H₂ activation. It was demonstrated that the methanol reaction intermediates formed on the metal oxide, then converted to lower olefins at the Brønsted acid sites in SAPO-34 zeolite [121]. Tong et al. developed a dual-function composite catalyst, 13%ZnO-ZrO₂/Mn_{0.1}SAPO-34, and attained a high CO₂ conversion of 21.3% with a light olefin selectivity of 61.7%, and suppressed the selectivity of CO below 43% and the CH₄ selectivity below 4%. The fine-tuned acidity of zeolite by the addition of Mn and the

granule stacking arrangement contributed to the excellent catalytic performance. Mn was embedded into the zeolite ionic structure to tune the acidity of the molecular sieve and limit secondary hydrogenation reactions. The granule stacking arrangement facilitated the tandem catalysis [122]. Dang et al. presented a series of bifunctional catalysts containing In-Zr composite oxides with different In/Zr atomic ratios and SAPO-34 zeolite for CO₂ conversion to light olefins. It was demonstrated that the inclusion of a certain amount of ZrO₂ could provide more oxygen vacancy sites (Figure 22a), stabilize the intermediates in the CO₂ hydrogenation, and prevent the sintering of the active nanoparticles. This, in turn, would lead to significantly enhanced catalytic activity, selectivity of hydrocarbons and stability for direct CO₂ hydrogenation to lower olefins at the relatively high reaction temperature of 653K. A light olefin selectivity as high as 80% at a CO₂ conversion rate of 27% and less than 2.5% methane selectivity was obtained over the optimized indium-zirconium/SAPO-34 bifunctional catalyst. The catalyst exhibited excellent stability for over 140 h without showing obvious deactivation (Figure 22b) [18].

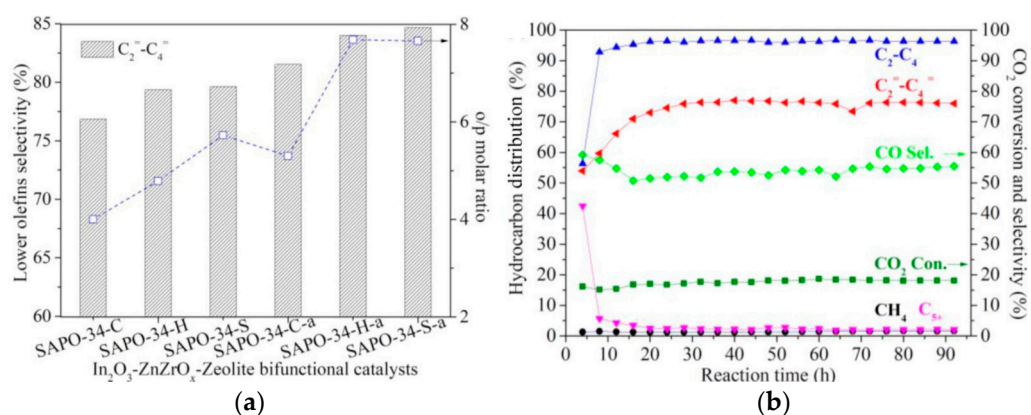


Figure 21. (a) Catalytic performance for CO₂ hydrogenation over a In₂O₃-ZnZrO_x catalyst with different types of SAPO-34. (b) The stability of the bifunctional composite catalysts In₂O₃-ZnZrO_x/SAPO-34-H-a (testing conditions: T = 653 K, P = 3.0 MPa, GHSV = 9000 mL_{g_{cat}}⁻¹h⁻¹, molar ratio of H₂/CO₂/N₂ = 73:24:3, mass ratio of oxide/zeolite = 0.5). Adapted with permission from ref. [42]. Copyright 2019 Wiley-VCH.

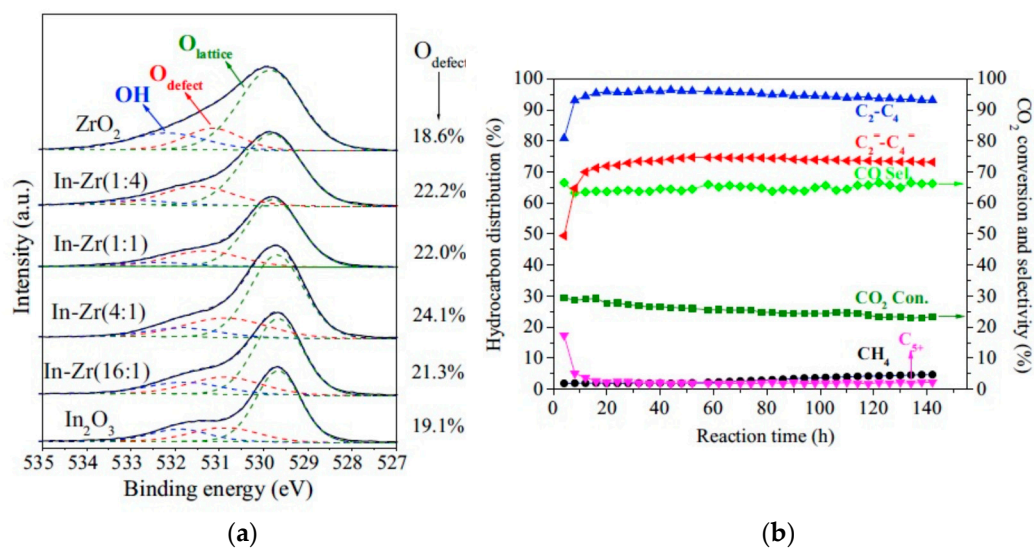


Figure 22. (a) XPS spectra (O1s) of various oxides and the content of surface oxygen vacancies (O_v). (b) The stability tests of the bifunctional composite catalysts In-Zr(4:1)/SAPO-34 (testing conditions: T = 653 K, P = 3.0 MPa, GHSV = 9000 mL_{g_{cat}}⁻¹ h⁻¹, molar ratio of H₂/CO₂/N₂ = 73/24/3, and mass ratio of oxide/zeolite = 0.5). Adapted with permission from ref. [18]. Copyright 2018 Elsevier.

In summary, the majority of the catalysts tested for CO₂ hydrogenation to light olefins via the MeOH-mediated route involve two active components (metal oxides and zeolite), which are so-called bifunctional composite catalysts. In this section, multiple variations (acidity, particle size, proximity, oxygen vacancy) in the combination of methanol synthesis catalysts (Cu, Zn, In, Ce, Zr, etc. metal oxides) with various zeolites (SAPO-34 and ZSM5) have been reported to give improved olefin selectivity and catalyst stability by mitigating coke formation, reducing the particle size growth of active carbide species, and inhibiting inactive species formation for CO₂ hydrogenation to light olefins.

3.4. Structure Effect

The structure of the catalysts plays an important role in converting CO₂ to light olefins. In this section, we will report the recent progress on the ways in which morphology changes in both the Fe-based and methanol zeolite composite catalysts can improve the catalytic performance. Some representative catalysts on the structure effect for CO₂ hydrogenation to light olefins with improved catalyst stability are presented in Table 4.

Table 4. Some representative catalysts on the structure effect for CO₂ hydrogenation to light olefins.

Catalyst	CO ₂ Conv., %	Selectivity, %				Yield, % C ₂ -C ₄ ⁼	O/P Ratio	Stability	Ref.
		CO	CH ₄	C ₂ -C ₄ ⁼	C ₂ -C ₄ ⁰				
0.8K-2.4Fe-1.3Ti	35.0	36.3	22.0	60.0	8.0	21.0	7.5	200 h	[123]
Fe@NC-400	29.0	17.5	27.0	21.0	12.0	6.1	1.7	>15 h	[36]
K/Fe-Al-O Spinel E.1 nanobelts	48.0	16.0	10.0	52.0	5.0	24.0	3.1	120 h	[124]
MgH ₂ /Cu _x O	20.7	n/a	40.0	54.8	7.0	11.3	7.8	210 h	[125]
CZA/SAPO-34	50.0	3.0	10.0	62.0	25.0	33.0	2.5	12 h	[126]
FeK1.5/HSG	50	39	31	56	9.9	28	5.7	>120 h	[127]
Carbon-confined MgH ₂ nano-lamellae	10.5	27.6	17.5	50.9	4.0	5.3	12.7	>2 h	[128]
Fe-Co/K-(CM-Al ₂ O ₃)	41.0	12.4	33.7	41.1	6.4	14.4	6.4	50 h	[37]
ZnO-Y ₂ O ₃ & SAPO-34	27.6	85.0	1.8	83.9 ^a	12.9 ^a	23.2	6.5	n/a	[40]
Cu-Zn-Al (6:3:1) oxide & HB zeolite	27.6	53.4	0.7	45.5 ^b	n/a	12.6 ^b	n/a	9 h	[129]

^a Refers to hydrocarbon distribution %; ^b refers to C₂-C₅⁺ hydrocarbons.

Wang et al. developed a layered metal oxides (LMO) structure, K-Fe-Ti, that displayed high catalytic activity, olefin selectivity and decent stability toward CO₂-FTS. The light olefin selectivity achieved approximately 60% with an olefin/paraffin ratio of 7.3 over the catalyst 0.8K-2.4Fe-1.3Ti (Figure 23). The LMO structure exfoliated through the acid treatment was found to weaken the interaction between Fe and Ti, which made it easier for the reduction and activation of iron oxides to form active iron carbide species that favored a shift from the RWGS to the FTS reaction. Meantime, C₂H₄ adsorption was hindered due to the low surface area of the LMO structure, contributing to higher olefin selectivity by inhibiting the secondary hydrogenation of primary olefins. The acid treatment played a key role in the formation of a slice structure that favored CO₂ conversion to light olefins with lower CO selectivity [123]. Fujiwara et al. found the composite catalysts obtained from the simple mixing of Cu-Zn-Al oxide together with HB zeolite, which was modified with 1,4-bis(hydroxydimethylsilyl) benzene, to be very effective for CO₂ hydrogenation to C₂⁺ hydrocarbons. The modification of zeolite with the disilane compound made the catalysts' surface hydrophobic, a characteristic which was effective in preventing catalyst deactivation by the formation of water during CO₂ hydrogenation. The highest yield of C₂⁺ hydrocarbons over the modified composite catalysts reached about 12.6 C-mol% at 573 K under a pressure of 0.98 Mpa. The diminishing of the deactivation of the strong acid sites of HB zeolite with the hydrophobic surface is the source of the enhanced catalytic activity [129].

Liu et al. synthesized a unique structure with ZnO and nitrogen-doped carbon (NC)-overcoated Fe-based catalysts (Fe@NC) (Figure 24), and found that the reaction rate increased by ~25%, while the O/P ratio increased from 0.07 to 1.68 when compared with the benchmark Fe₃O₄ catalyst. The inactive θ-Fe₃C phase disappeared, and the active phases (Fe₃O₄ and Fe₅C₂) formed for CO₂ hydrogenation. The introduction of NC to the

surface of the Fe catalysts significantly boosted the catalyst activity, the selectivity toward light olefins, and the stability due to the enhanced metal–support–reactant interaction and interfacial charge transfer [36].

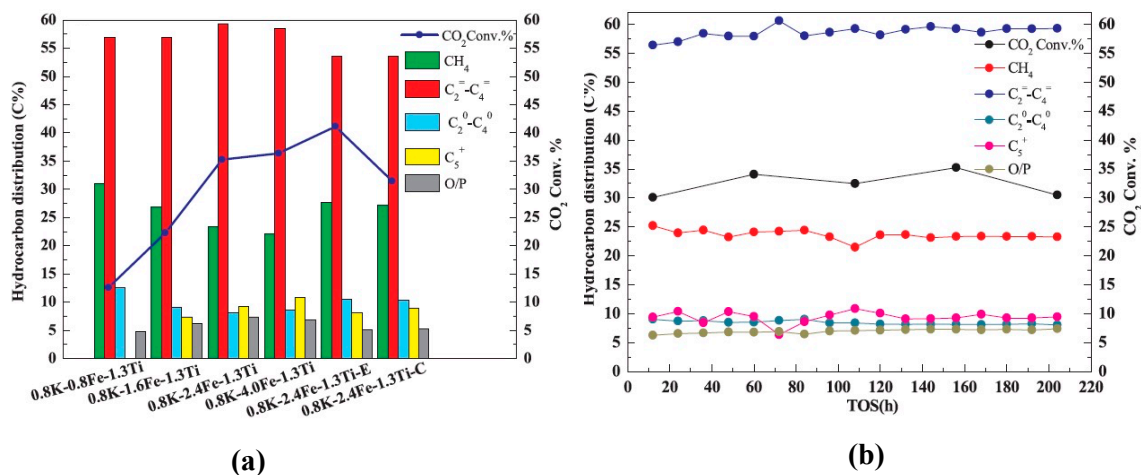


Figure 23. (a) Catalytic performance over different catalysts. (b) The catalytic stability of 0.8K-2.4Fe-1.3Ti at TOS (testing conditions: H₂/CO₂ molar ratio = 3/1, T = 593 K, P = 2.0 MPa and GHSV = 10,000 mL gcat⁻¹h⁻¹). Adapted with permission from ref. [123]. Copyright 2019 Elsevier.

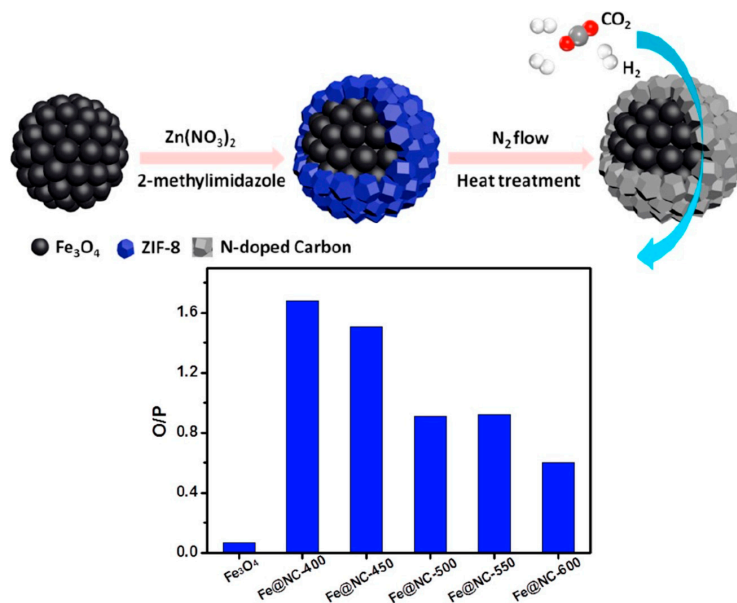


Figure 24. Schematic illustration of the formation of Fe@NC catalysts and the reaction for CO₂ hydrogenation. Adapted with permission from ref. [36]. Copyright 2019 American Chemical Society.

Numpilai et al. studied the hydrogenation of CO₂ to light olefins over Fe-Co/K-Al₂O₃ catalysts, and discovered that the pore sizes of the Al₂O₃ support had profound effects on the Fe₂O₃ crystallite size, the reducibility, the adsorption–desorption of CO₂ and H₂, and the catalytic performances. The highest olefins to paraffins ratio of 6.82 was obtained from the largest pore catalyst (CL-Al₂O₃) due to the suppression of the hydrogenation of olefins to paraffins by increasing the pore sizes of Al₂O₃ to eliminate diffusion limitation. The maximum light olefin yield of 14.38% was obtained over the catalyst with an appropriated Al₂O₃ pore size (49.7 nm) owing to the suppression of the olefins' hydrogenation and chain growth reaction [37].

The electrospun ceramic K/Fe-Al-O nanobelt catalysts synthesized by Elishav et al. showed a much higher CO₂ conversion of 48%, a C₂-C₅ olefin selectivity of 52%, and a high olefin/paraffin ratio of 10.4, while the K/Fe-Al-O spinel powder catalyst produced mainly

C₆₊ hydrocarbons. The enhanced olefin selectivity of the electrospun materials is related to a high degree of reduction of the surface Fe atoms due to the more efficient interaction with the K promoter [124].

A defect-rich MgH₂/Cu_xO hydrogen storage composite might inspire the catalysts' design for the hydrogenation of CO₂ to lower olefins. Chen et al. presented a defect-rich MgH₂/Cu_xO composite catalyst that achieved a C₂[−]–C₄[−] selectivity of 54.8% and a CO₂ conversion of 20.7% at 623 K under a low H₂/CO₂ ratio of 1:5. It is the defective structure of MgH₂/Cu_xO that promotes CO₂ molecule adsorption and activation, while the electronic structure of MgH₂ was more conducive to the provision of lattice H[−] for the hydrogenation of the CO₂ molecule. The lattice H[−] could combine with the C site of the CO₂ molecule to promote the formation of Mg formate, which was further hydrogenated to lower olefins under a low H[−] concentration [125]. The same group reported carbon-confined MgH₂ nano-lamellae which stored solid hydrogen for the hydrogenation of CO₂ to lower olefins and demonstrated a high selectivity under low H₂/CO₂ ratios. The high selectivity of lower olefins was attributed to the low concentration of solid hydrogen under low H₂/CO₂ ratios that suppressed the further hydrogenation of light olefins from Mg formate [128].

SAPO-34 molecular sieves were considered to be the best catalysts due to their excellent structure selectivity, suitable acidity, favorable thermal stability, and hydrothermal stability, as well as their high selectivity for light olefins. Tian et al. used Palygorskite as a silicon and partial aluminum source, and DEA, TEA, MOR and TEOH as template agents to prepare SAPO-34 molecular sieves with higher purity. Composite catalysts of CuO-ZnO-Al₂O₃/SAPO-34 were prepared by mechanically mixing SAPO-34 molecular sieves with CuO-ZnO-Al₂O₃ (CZA), and a superb CO₂ conversion of 53.5%, a light olefin selectivity of 62.1% and a yield of 33.2% were obtained over the CZA/SAPO-34(TEOH)HCl composite catalyst [126]. CO₂ conversion and product distribution are strongly dependent on the oxide composition and structure. Li et al. developed a bifunctional catalyst composed of ZnO-Y₂O₃ oxide and SAPO-34 zeolite that offered a CO₂ conversion of 27.6% and a light olefin selectivity of 83.6% [40].

Some Fe-containing catalysts can also be improved by creating unique architectures. Wei et al. created Fe-based catalysts with honeycomb-structured graphene (HSG) as the catalyst support and K as the promoter, and achieved the 59% selectivity of light olefins over a FeK_{1.5}/HSG catalyst. No obvious deactivation was observed within 120 h on stream (Figure 25). The excellent catalytic performance was ascribed to the confinement effect of HSG and the K promotion effect on the activation of inert CO₂ and the formation of iron carbide. The complex three-dimensional (3D) architecture of the porous HSG effectively impeded the sintering of the active sites' iron carbide nanoparticles (NPs). Meanwhile, CO₂ and H₂ could more easily permeate the mesoporous–macroporous framework of HSG and access the catalysts' active sites. Similarly, the generated light olefins could more easily emerge from the catalyst so as to avoid further unwanted hydrogenation [127].

Consequently, multiple reports indicate that the modification of the morphology of zeolite–methanol synthesis composites by creating core–shell configurations can have a beneficial effect [16,120,130]. For example, dual-function composite catalysts containing CuZnZr (CZZ) and SAPO-34 were synthesized by Chen et al. for the tandem reactions of CO₂ to methanol and methanol to olefins. The assembled core–shell CZZ@SAPO-34 catalyst, as shown in Figure 26, exhibited an enhanced light olefin selectivity of 72% and inhibited CH₄ formation due to reduced contact interface between CZZ and SAPO-34 and weakened hydrogenation ability at the metal sites. Furthermore, the addition of Zn reduced the acidity of SAPO-34; as a result, the secondary reactions of the primary olefins were significantly diminished (Figure 26) [120].

In summary of this section, the structure and the properties associated with the structure of the catalysts are pivotal for CO₂ hydrogenation to light olefins. The low surface area of the LMO structure could hinder the C₂H₄ secondary reaction, contributing to higher olefin selectivity. The surface modification of zeolite from hydrophilic to hydrophobic could prevent the catalyst deactivation caused by the formation of water. The unique structure of

Fe@NC enables phase transformation from the inactive (θ -Fe₃C) phase to active species (Fe₃O₄ and Fe₅C₂). Increasing the pore sizes of Al₂O₃ could eliminate the diffusion limitation for CO₂ and H₂. The electrospun ceramic K/Fe-Al-O nanobelt catalysts led to a high degree of the reduction of surface iron atoms. The defective structure of MgH₂/Cu_xO and carbon-confined MgH₂/C nano-lamellae could promote CO₂ adsorption and activation, with the electronic structure of MgH₂ offering lattice H⁻ for CO₂ hydrogenation. The 3D architecture of the porous HSG could impede the sintering of the active sites' iron carbide NPs. The confinement of core-shell CZZ@SAPO-34 structure could increase the access frequency of the methanol intermediate to the active zeolite sites, consequently improving the light olefine selectivity.

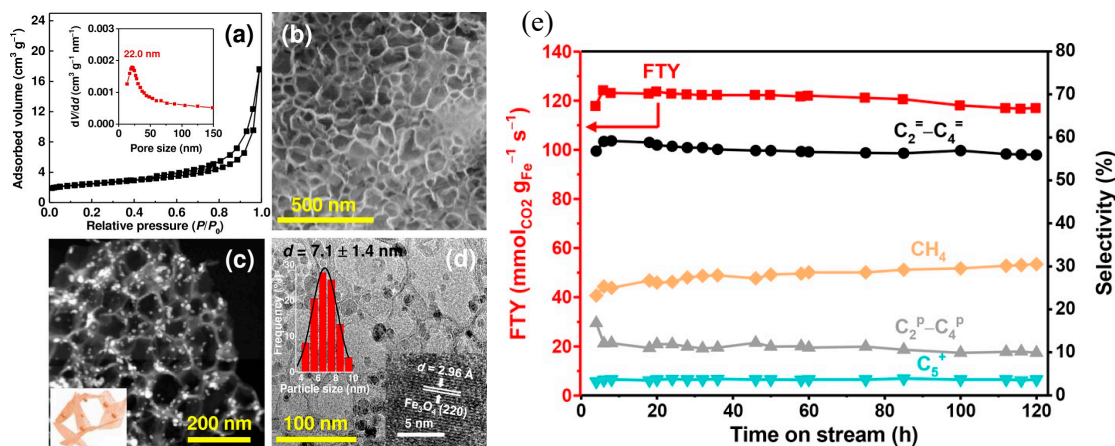


Figure 25. (a) N₂ physisorption isotherms, (b) SEM image, (c) HAADF–STEM image, and (d) TEM image and particle distribution of the FeK1.5/HSG catalyst. (e) CO₂ hydrogenation over the catalyst FeK1.5/HSG during a TOS of 120 h (testing conditions: mass of catalyst = 0.15 g, T = 613 K, P = 20 bar, H₂/CO₂ molar ratio = 3, and GHSV = 26 L h⁻¹g⁻¹). Adapted with permission from ref. [127]. Copyright 2018 American Chemical Society.

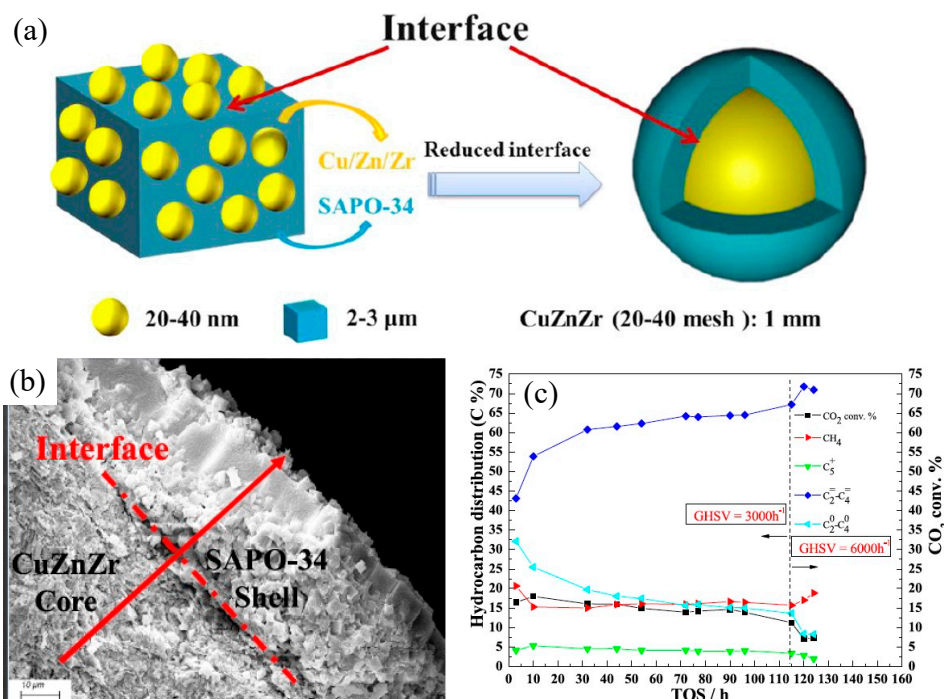


Figure 26. (a) Schematic illustration of the interface between CZZ and SAPO-34. (b) Core–shell interface of CZZ and SAPO-34. (c) Stability of the composite catalyst CZZ@Zn-SAPO-34 at TOS (testing conditions: H₂/CO₂ molar ratio = 3, T = 673 K). Adapted with permission from ref. [120]. Copyright 2019 Elsevier.

4. Conclusions

There is an urgent need to control CO₂ emissions in order to mitigate their negative impact on the environment. The catalytic conversion of CO₂ is an encouraging approach to mitigate CO₂ emissions by producing chemicals and fuels. A highly promising route is selective CO₂ hydrogenation to produce light olefins. The huge market demand for the lower olefins offers a great opportunity for the target technology to profoundly impact the scale of CO₂ utilization once it is developed with renewable hydrogen. Currently, there are two primary pathways (the CO₂–FTS route and the MeOH-mediated route) to produce light olefins from CO₂ hydrogenation in a one-step process. In the CO₂–FTS path, Fe is one of the most widely used components, while in the MeOH path, Cu/zeolite has been used the most. Even though significant efforts have been made, considerable challenges remain in the development of highly efficient catalysts with selective pathways to light olefins due to the thermodynamically stable nature of the CO₂ molecule, the complexity of the reaction networks, and catalyst deactivation. During CO₂ hydrogenation, the primary causes for catalyst deactivation are the sintering (or agglomeration) of metal particles, phase transformation at the catalyst's surface, and catalyst poisoning by water or carbonaceous deposits (i.e., coke). A firm grasp of the causes for deactivation is essential in order to develop a mitigation strategy and sustain a high selectivity toward the desired olefins during CO₂ hydrogenation. In this review, we summarized the reports published within five years on the effect of the promoters, metal oxide support, bifunctional composites and structure on the catalyst design in order to minimize catalyst deactivation.

Promoter effect: Alkali metals such as K and Na have been broadly used as promoters to control the electronic properties. Mn, Ce, and Ca metals have been used as structural promoters. Transition metals such as Zn, Co, Cu, V, Zr, etc., have been used as both electronic and structural promoters. With the inclusion of alkali promoters, Fe-based catalysts can possess higher olefin selectivity. The alkali metals act as electron donors to Fe metal centers, fostering CO₂ adsorption while decreasing their affinity with H₂, and consequently leading to a higher olefin yield. Some studies show that doping the catalyst with a second metal improves the olefin yield by forming a highly active interface. The second metal promoters may provide a way to tune the CO₂ and H₂ adsorption and activation, shifting the product distribution towards the desired hydrocarbons.

Support effect: Supporting the Fe-based species on supports such as SiO₂, CeO₂, m-ZrO₂, γ-Al₂O₃, TiO₂, ZSM-5, MgO, NbO HPCMs, MOFs, and β-Mo₂C may enhance the catalytic performance by improving the active metal dispersion and retarding the sintering of the active particles. The surface area, basicity, reducibility, oxygen vacancies, and morphology of the support played important roles—in most cases, with the presence of promoters (K, Zr, Cs)—in affecting the amount and particle size of the active carbide species; the synergy effect; the metal–support interaction; the strength and capacity of CO, CO₂, and H₂ adsorption on support; and the surface C/H ratio for CO₂ hydrogenation. By tuning the above-mentioned characteristics properly, the physically deposited carbon species, coke generation and metal sintering could be mitigated.

Bifunctional composite catalyst effect: The catalysts tested for CO₂ hydrogenation to light olefins via the MeOH-mediated route mainly involve two active components (metal oxides and zeolite), and so are called bifunctional composite catalysts. In this review, multiple variations (acidity, particle size, proximity, oxygen vacancy) of the combination of methanol synthesis catalysts (Cu, Zn, In, Ce, Zr, etc. metal oxides) with various zeolites (SAPO-34 and ZSM5) have been reported for enhanced olefin selectivity and catalyst stability by mitigating coke formation, reducing the particle size growth of active carbide species, and inhibiting inactive species formation for CO₂ hydrogenation to light olefins.

Structure effect: The structure of the catalysts plays a pivotal role in CO₂ hydrogenation to light olefins. The structures and properties (for example, LMO, the surface modification of zeolite from hydrophilic to hydrophobic, Fe@NC, the pore sizes of Al₂O₃, the defective structure of MgH₂/Cu_xO and carbon-confined MgH₂/C nano-lamellae, the 3D architecture of the porous HSG, and core–shell CZZ@SAPO-34) could be tuned to mitigate catalyst

deactivation by retarding the sintering of active species and coke deposition, tolerating water formation and enabling favorable phase transformation for an enhanced light olefin yield and catalyst stability.

Despite the many advances made in catalytic development, especially with light olefin yield and stability, a novel catalytic system that is both economically viable and resistant to deactivation has not yet been achieved. Most research efforts have focused on the development of catalytic materials and the adjustment of properties and metal interactions for the desired catalyst activity and long-term stability. Future research directions for CO₂ hydrogenation should consider: (1) the further modification of the catalytic surface H/C molar ratio and the fostering of C-C coupling; (2) tuning the basicity and oxygen vacancies of the catalyst support to facilitate the CO₂ adsorption and activation; (3) examining more novel catalytic materials/structures to boost the catalyst stability; and (4) exploring more energy-saving catalysts for CO₂ hydrogenation to light olefins. In addition, in situ measurements using synchrotron-based techniques, such as X-ray adsorption spectroscopy (XAS), should be performed in order to understand the ways in which the local environment of the catalysts affects their activity, stability and efficient mitigation.

Author Contributions: Conceptualization, C.Z.; writing—original draft, C.Z., N.J.R., T.H., D.W., M.W., C.M., A.Z. and N.F.; writing—review and editing, C.Z. and N.J.R.; funding acquisition, C.Z.; resources, C.Z.; supervision, C.Z. All authors have read and agreed to the published version of the manuscript.

Funding: This work was supported by the National Science Foundation under Grant No. 1955521 (C.Z.).

Acknowledgments: The authors are grateful for the U.S. Department of Energy, the Office of Science, and the Office of Workforce Development for Teachers and Scientists under the Science Undergraduate Laboratory Internships Program (T.H. and A.Z.) and Visiting Faculty Program (C.Z.).

Conflicts of Interest: The authors declare no conflict of interest.

Abbreviations

FTS	Fisch–Tropsch Synthesis
MeOH	methanol
RWGS	reverse water–gas shift
MTO	MeOH-to-olefins
ASF	Anderson–Schulz–Flory
CTO	CO ₂ to olefins
XRD	X-ray powder diffraction
PFR	plug-flow
CSTR	fully back-mixed reactors
TPSR	Temperature-programed surface reaction
XPS	X-ray photoelectron spectroscopy
SEM	scanning electron microscopy
TEM	transmission electron microscopy
HAADF–STEM	high-angle annular dark-field-scanning transmission electron microscopy
O/P ratio	olefins/paraffin ratio
NPs	nanoparticles
CNT	carbon nanotubes
FTY	Fe time yield
STY	space–time yields
HPCMs	hierarchical porous carbon monoliths
LMO	layered metal oxides
MOF	metal organic framework

References

1. Zhang, X.; Zhang, A.; Jiang, X.; Zhu, J.; Liu, J.; Li, J.; Zhang, G.; Song, C.; Guo, X. Utilization of CO₂ for aromatics production over ZnO/ZrO₂-ZSM-5 tandem catalyst. *J. CO₂ Util.* **2019**, *29*, 140–145. [CrossRef]
2. Atmospheric CO₂ Levels Defy the Pandemic to Hit Record High. Available online: <https://newatlas.com/environment/atmospheric-co2-pandemic-record-concentrations/> (accessed on 15 October 2021).
3. Monastersky, R. Global carbon dioxide levels near worrisome milestone. *Nature* **2013**, *497*, 13–14. [CrossRef] [PubMed]
4. Da Silva, I.A.; Mota, C. Conversion of CO₂ to light olefins over iron-based catalysts supported on niobium oxide. *Front. Energy Res.* **2019**, *7*, 49. [CrossRef]
5. Keith, D.; Holmes, G.; Angelo, D.S.; Heidel, K. A process for capturing CO₂ from the atmosphere. *Joule* **2018**, *2*, 1573–1594. [CrossRef]
6. Centi, G.; Quadrelli, E.A.; Perathoner, S. Catalysis for CO₂ conversion: A key technology for rapid introduction of renewable energy in the value chain of chemical industries. *Energy Environ. Sci.* **2013**, *6*, 1711. [CrossRef]
7. Dutta, A.; Farooq, S.; Karimi, I.A.; Khan, S.A. Assessing the potential of CO₂ utilization with an integrated framework for producing power and chemicals. *J. CO₂ Util.* **2017**, *19*, 49–57. [CrossRef]
8. Ma, Z.; Porosoff, M. Development of tandem catalysts for CO₂ hydrogenation to olefins. *ACS Catal.* **2019**, *9*, 2639–2656. [CrossRef]
9. Science Daily. Available online: <https://www.sciencedaily.com/releases/2018/11/181108130533.htm> (accessed on 15 August 2021).
10. Li, W.; Zhang, G.; Jiang, X.; Liu, Y.; Zhu, J.; Ding, F.; Liu, Z.; Guo, X.; Song, C. CO₂ hydrogenation on un-promoted and M-promoted Co/TiO₂ catalysts (M = Zr, K, Cs): Effects of crystal phase of supports and metal–support interaction on tuning product distribution. *ACS Catal.* **2019**, *9*, 2739–2751. [CrossRef]
11. Wei, J.; Yao, R.W.; Ge, Q.J.; Wen, Z.Y.; Ji, X.W.; Fang, C.Y.; Zhang, J.X.; Xu, H.Y.; Sun, J. Catalytic hydrogenation of CO₂ to isoparaffins over Fe-based multifunctional catalysts. *ACS Catal.* **2018**, *8*, 9958–9967. [CrossRef]
12. Wei, J.; Ge, Q.; Yao, R.; Wen, Z.; Fang, C.; Guo, L.; Xu, H.; Sun, J. Directly converting CO₂ into a gaso-line fuel. *Nat. Commun.* **2018**, *8*, 15174. [CrossRef]
13. Li, Z.; Wang, J.; Qu, Y.; Liu, H.; Tang, C.; Miao, S.; Feng, Z.; An, H.; Li, C. Highly selective conversion of carbon dioxide to lower olefins. *ACS Catal.* **2017**, *7*, 8544–8548. [CrossRef]
14. Li, Z.L.; Qu, Y.Z.; Wang, J.J.; Liu, H.L.; Li, M.R.; Miao, S.; Li, C. Highly selective conversion of carbon dioxide to aromatics over tandem catalysts. *Joule* **2019**, *3*, 570–583. [CrossRef]
15. Liu, J.H.; Zhang, A.F.; Jiang, X.; Liu, M.; Zhu, J.; Song, C.S.; Guo, X.W. Direct transformation of carbon dioxide to value-added hydrocarbons by physical mixtures of Fe₅C₂ and K-modified Al₂O₃. *Ind. Eng. Chem. Res.* **2018**, *57*, 9120–9126. [CrossRef]
16. Xie, C.L.; Chen, C.; Yu, Y.; Su, J.; Li, Y.F.; Somorjai, G.A.; Yang, P.D. Tandem catalysis for CO₂ hydrogenation to C₂–C₄ hydrocarbons. *Nano Lett.* **2017**, *17*, 3798–3802. [CrossRef] [PubMed]
17. Liu, M.; Yi, Y.H.; Wang, L.; Guo, H.C.; Bogaerts, A. Hydrogenation of carbon dioxide to value-added chemicals by heterogeneous catalysis and plasma catalysis. *Catalysts* **2019**, *9*, 275. [CrossRef]
18. Dang, S.S.; Gao, P.; Liu, Z.Y.; Chen, X.Q.; Yang, C.G.; Wang, H.; Zhong, L.S.; Li, S.G.; Sun, Y.H. Role of zirconium in direct CO₂ hydrogenation to lower olefins on oxide/zeolite bifunctional catalysts. *J. Catal.* **2018**, *364*, 382–393. [CrossRef]
19. Gao, P.; Dang, S.S.; Li, S.G.; Bu, X.N.; Liu, Z.Y.; Qiu, M.H.; Yang, C.G.; Wang, H.; Zhong, L.S.; Han, Y.; et al. Direct production of lower olefins from CO₂ conversion via bifunctional catalysis. *ACS Catal.* **2018**, *8*, 571–578. [CrossRef]
20. Saeidi, S.; Najari, S.; Hessel, V.; Wilson, K.; Keil, F.J.; Concepción, P.; Suib, S.L.; Rodrigues, A.E. Recent advances in CO₂ hydrogenation to value-added products—Current challenges and future directions. *Prog. Energy Combust. Sci.* **2021**, *85*, 100905. [CrossRef]
21. Gnanamani, M.K.; Jacobs, G.; Hamdeh, H.H.; Shafer, W.D.; Liu, F.; Hopps, S.D.; Thomas, G.A.; Davis, B.H. Hydrogenation of carbon dioxide over Co–Fe bimetallic catalysts. *ACS Catal.* **2016**, *6*, 913–927. [CrossRef]
22. Ren, T.; Patel, M.; Blok, K. Olefins from conventional and heavy feedstocks: Energy use in steam cracking and alternative processes. *Energy* **2006**, *31*, 425–451. [CrossRef]
23. Amghizar, I.; Vandewalle, L.A.; Geem, K.M.V.; Marin, G.B. New trends in olefin production. *Engineering* **2017**, *3*, 171–178. [CrossRef]
24. One, O.; Niziolek, A.M.; Floudas, C.A. Optimal production of light olefins from natural gas via the methanol intermediate. *Ind. Eng. Chem. Res.* **2016**, *55*, 3043–3063.
25. Li, W.H.; Wang, H.Z.; Jiang, X.; Zhu, J.; Liu, Z.M.; Guo, X.W.; Song, C.S. A short review of recent advances in CO₂ hydrogenation to hydrocarbons over heterogeneous catalysts. *RCS Adv.* **2018**, *8*, 7651–7669. [CrossRef]
26. Porosoff, M.; Yan, B.; Chen, J. Catalytic reduction of CO₂ by H₂ for synthesis of CO, methanol and hydrocarbons: Challenges and opportunities. *Energy Environ. Sci.* **2016**, *9*, 62–73. [CrossRef]
27. Wang, D.; Xie, Z.; Porosoff, M.D.; Chen, J. Recent advances in carbon dioxide hydrogenation to produce olefins and aromatics. *Chem* **2021**, *7*, 1–35. [CrossRef]
28. Zhang, C.; Cao, C.; Zhang, Y.; Liu, X.; Xu, J.; Zhu, M.; Tu, W.; Han, Y. Unraveling the role of zinc on bimetallic Fe₅C₂–ZnO catalysts for highly selective carbon dioxide hydrogenation to high carbon α -olefins. *ACS Catal.* **2021**, *11*, 2121–2133. [CrossRef]
29. Wang, X.; Zhang, J.; Chen, J.; Ma, Q.; Fan, S.; Zhao, T.S. Effect of preparation methods on the structure and catalytic performance of Fe–Zn/K catalysts for CO₂ hydrogenation to light olefins. *Chin. J. Chem. Eng.* **2018**, *26*, 761–767. [CrossRef]

30. Numpilai, T.; Cheng, C.K.; Limtrakul, J.; Witoon, T. Recent advances in light olefins production from catalytic hydrogenation of carbon dioxide. *Proc. Saf. Environ. Prot.* **2021**, *151*, 401–427. [[CrossRef](#)]
31. Wei, J.; Sun, J.; Wen, Z.; Fang, C.; Ge, Q.; Xu, H. New insights into the effect of sodium on Fe₃O₄-based nano-catalysts for CO₂ hydrogenation to light olefins. *Catal. Sci. Technol.* **2016**, *6*, 4786. [[CrossRef](#)]
32. Wezendonk, T.A.; Sun, X.; Duglan, A.I.; van Hoof, A.J.F.; Hensen, E.J.M.; Kapteijn, F.; Gascon, J. Controlled formation of iron carbides and their performance in Fischer-Tropsch synthesis. *J. Catal.* **2018**, *362*, 106–117. [[CrossRef](#)]
33. Chaipraditgul, N.; Numpilai, T.; Cheng, C.K.; Siri-Nguan, N.; Sornchamni, T.; Wattanakit, C.; Limtrakul, J.; Witoon, T. Tuning interaction of surface-adsorbed species over Fe/K-Al₂O₃ modified with transition metals (Cu, Mn, V, Zn or Co) on light olefins production from CO₂ hydrogenation. *Fuel* **2021**, *283*, 119248. [[CrossRef](#)]
34. Gnanamani, M.K.; Jacobs, G.; Hamdeh, H.H.; Shafer, W.D.; Liu, F.; Hopps, S.D.; Thomas, G.A.; Davis, B.H. Hydrogenation of carbon dioxide over iron carbide prepared from alkali metal promoted iron oxalate. *Appl. Catal. A Gen.* **2018**, *564*, 243–249. [[CrossRef](#)]
35. Guo, L.; Sun, J.; Ge, Q.; Tsubaki, N. Recent advances in direct catalytic hydro-genation of carbon dioxide to valuable C₂+ hydrocarbons. *J. Mater. Chem. A* **2018**, *6*, 23244–23262. [[CrossRef](#)]
36. Liu, J.; Zhang, A.; Jiang, X.; Zhang, G.; Sun, Y.; Liu, M.; Ding, F.; Song, C.; Guo, X. Overcoating the surface of Fe-based catalyst with ZnO and nitrogen-doped carbon toward high selectivity of light olefins in CO₂ Hydrogenation. *Ind. Eng. Chem. Res.* **2019**, *58*, 4017–4023. [[CrossRef](#)]
37. Numpilai, T.; Chanel, N.; Poo-Arporn, Y.; Cheng, C.; Siri-Nguan, N.; Sornchamni, T.; Chareonpanich, M.; Kongkachuichay, P.; Yigit, N.; Rupprechter, G.; et al. Pore size effects on physicochemical properties of Fe-Co/K-Al₂O₃ catalysts and their catalytic activity in CO₂ hydrogenation to light olefins. *Appl. Surf. Sci.* **2019**, *483*, 581–592. [[CrossRef](#)]
38. Yang, H.; Zhang, C.; Gao, P.; Wang, H.; Li, X.; Zhong, L.; Wei, W.; Sun, Y. A review of the catalytic hydro-genation of carbon dioxide into value-added hydrocarbons. *Catal. Sci. Technol.* **2017**, *7*, 4580. [[CrossRef](#)]
39. Jiao, F.; Li, J.; Pan, X.; Xiao, J.; Li, H.; Ma, H.; Wei, M.; Pan, Y.; Zhou, Z.; Li, M.; et al. Selective conversion of syngas to light olefins. *Science* **2016**, *351*, 1065–1068. [[CrossRef](#)] [[PubMed](#)]
40. Li, J.; Yu, T.; Miao, D.; Pan, X.; Bao, X. Carbon dioxide hydrogenation to light olefins over ZnO/Y₂O₃ and SAPO-34 bifunctional catalysts. *Catal. Commun.* **2019**, *129*, 105711. [[CrossRef](#)]
41. Liu, X.; Wang, M.; Zhou, C.; Zhou, W.; Cheng, K.; Kang, J.; Zhang, Q.; Deng, W.; Wang, Y. Selective transformation of carbon dioxide into lower olefins with a bifunctional catalyst composed of ZnGa₂O₄ and SAPO-34. *Chem. Commun.* **2018**, *54*, 140–143. [[CrossRef](#)]
42. Dang, S.; Li, S.; Yang, C.; Chen, X.; Li, X.; Zhong, L.; Gao, P.; Sun, Y. Selective transformation of CO₂ and H₂ into lower olefins over In₂O₃-ZnZrOx/SAPO-34 bifunctional catalysts. *ChemSusChem* **2019**, *12*, 3582–3591. [[CrossRef](#)]
43. Gao, J.; Jia, C.; Liu, B. Direct and selective hydrogenation of CO₂ to ethylene and propene by bifunctional catalysts. *Catal. Sci. Technol.* **2017**, *7*, 5602–5607. [[CrossRef](#)]
44. Tan, L.; Zhang, P.; Cui, Y.; Suzuki, Y.; Li, H.; Guo, L.; Yang, G.; Tsubaki, N. Direct CO₂ hydrogenation to light olefins by suppressing CO by-product formation. *Fuel Process. Technol.* **2019**, *196*, 106174–106178. [[CrossRef](#)]
45. Porosoff, M.D.; Kattel, S.; Li, W.; Liu, P.; Chen, J.G. Identifying trends and descriptors for selective CO₂ conversion to CO over transition metal carbides. *Chem. Commun.* **2015**, *51*, 6988–6991. [[CrossRef](#)] [[PubMed](#)]
46. Porosoff, M.D.; Chen, J.G. Trends in the catalytic reduction of CO₂ by hydrogen over supported monometallic and bimetallic catalysts. *J. Catal.* **2013**, *301*, 30–37. [[CrossRef](#)]
47. Butt, J.B.; Petersen, E. *Activation, Deactivation and Poisoning of Catalysts*; Academic Press: Cambridge, MA, USA, 1988.
48. Bartholomew, C. Mechanisms of catalyst deactivation. *Appl. Catal. A Gen.* **2001**, *212*, 17–60. [[CrossRef](#)]
49. Moulijn, J.A.; van Diepen, A.E.; Kapteijn, F. Catalyst deactivation: Is it predictable? What to do? *Appl. Catal. A Gen.* **2001**, *212*, 3–16. [[CrossRef](#)]
50. Price, C.A.H.; Reina, T.R.; Liu, J. Engineering heterogeneous catalysts for chemical CO₂ utilization: Lessons from thermal catalysis and advantages of yolk@shell structured nanoreactors. *J. Energy Chem.* **2021**, *57*, 304–324. [[CrossRef](#)]
51. Kliewer, C.E.; Soled, S.L.; Kiss, G. Morphological transformations during Fischer-Tropsch synthesis on a titania-supported cobalt catalyst. *Catal. Today* **2019**, *323*, 233–256. [[CrossRef](#)]
52. Eschemann, T.O.; de Jong, K.P. Deactivation behavior of Co/TiO₂ catalysts during Fischer-Tropsch synthesis. *ACS Catal.* **2015**, *5*, 3181–3188. [[CrossRef](#)]
53. Sun, J.T.; Metcalfe, I.S.; Sahibzada, M. Deactivation of Cu/ZnO/Al₂O₃ methanol synthesis catalyst by sintering. *Ind. Eng. Chem. Res.* **1999**, *38*, 3868–3872. [[CrossRef](#)]
54. Argyle, M.; Bartholomew, C. Heterogeneous catalyst deactivation and regeneration: A review. *Catalysts* **2015**, *5*, 145–269. [[CrossRef](#)]
55. Hansen, T.W.; Delariva, A.T.; Challa, S.R.; Datye, A.K. Sintering of catalytic nanoparticles: Particle migration or Ostwald ripening. *Acc. Chem. Res.* **2013**, *46*, 1720–1730. [[CrossRef](#)] [[PubMed](#)]
56. Li, W.; Zhang, A.; Jiang, X.; Janik, M.J.; Qiu, J.; Liu, Z.; Guo, X.; Song, C. The anti-sintering catalysts: Fe-Co-Zr polymetallic fibers for CO₂ hydrogenation to C₂–C₄ rich hydrocarbons. *J. CO₂ Util.* **2018**, *23*, 219–225. [[CrossRef](#)]
57. Lee, S.-C.; Kim, J.-S.; Shin, W.C.; Choi, M.-J.; Choung, S.-J. Catalyst deactivation during hydrogenation of carbon dioxide: Effect of catalyst position in the packed bed reactor. *J. Mol. Catal. A Chem.* **2009**, *301*, 98–105. [[CrossRef](#)]

58. Riedel, T.; Schulz, H.; Schaub, G.; Jun, K.W.; Hwang, J.S.; Lee, K.W. Fischer–Tropsch on iron with H₂–CO and H₂–CO₂ as synthesis gases: The episodes of formation of the Fischer–Tropsch regime and construction of the catalyst. *Top. Catal.* **2003**, *26*, 41–54. [[CrossRef](#)]
59. Wang, W.; Wang, S.P.; Ma, X.B.; Gong, J.L. Recent advances in catalytic hydrogenation of carbon dioxide. *Chem. Soc. Rev.* **2011**, *40*, 3703–3727. [[CrossRef](#)]
60. Zhang, Y.; Cao, C.; Zhang, C.; Zhang, Z.; Liu, X.; Yng, Z.; Zhu, M.; Meng, B.; Jing, X.; Han, Y.-F. The study of structure-performance relationship of iron catalyst during a full life cycle for CO₂ hydrogenation. *J. Catal.* **2019**, *378*, 51–62. [[CrossRef](#)]
61. Fiato, R.A.; Rice, G.W.; Miseo, S.; Soled, S.L. Laser Produced Iron Carbide-Based Catalysts. U.S. Patent 4,687,753, 18 August 1987.
62. Hegedus, L.L.; McCabe, R.W. Catalyst Poisoning. In *Catalyst Deactivation 1980 (Studies in Surface Science and Catalysis)*; Delmon, B., Froment, G.F., Eds.; Elsevier: Amsterdam, The Netherlands, 1980; Volume 6, pp. 471–505.
63. Bartholomew, C.H. Mechanisms of nickel catalyst poisoning. In *Catalyst Deactivation 1987 (Studies in Surface Science and Catalysis)*; Delmon, B., Froment, G.F., Eds.; Elsevier: Amsterdam, The Netherlands, 1987; Volume 34, pp. 81–104.
64. Schühle, P.; Schmidt, M.; Schill, L.; Rilsager, A.; Wasserscheid, P.; Albert, J. Influence of gas impurities on the hydrogenation of CO₂ to methanol using indium-based catalysts. *Catal. Sci. Technol.* **2020**, *10*, 7309–7322. [[CrossRef](#)]
65. Szailer, T.; Novák, É.; Oszkó, A.; Erdőhelyi, A. Effect of H₂S on the hydrogenation of carbon dioxide over supported Rh catalysts. *Top. Catal.* **2007**, *46*, 79–86. [[CrossRef](#)]
66. Rytter, E.; Holmen, A. Perspectives on the effect of water in cobalt Fischer–Tropsch synthesis. *ACS Catal.* **2017**, *7*, 5321–5328. [[CrossRef](#)]
67. Wu, J.; Luo, S.; Toyir, J.; Saito, M.; Takeuchi, M.; Watanabe, T. Optimization of preparation conditions and improvement of stability of Cu/ZnO-based multicomponent catalysts for methanol synthesis from CO₂ and H₂. *Catal. Today* **1998**, *45*, 215–220. [[CrossRef](#)]
68. Wu, J.; Saito, M.; Takeuchi, M.; Watanabe, T. The stability of Cu/ZnO-based catalysts in methanol synthesis from a CO₂-rich feed and from a CO-rich feed. *Appl. Catal. A Gen.* **2001**, *218*, 235–240. [[CrossRef](#)]
69. Huber, G.W.; Guymon, C.G.; Conrad, T.L.; Stephenson, B.C.; Bartholomew, C.H. Hydrothermal stability of Co/SiO₂ Fischer–Tropsch Synthesis Catalysts. *Stud. Surf. Sci. Catal.* **2001**, *139*, 423–429.
70. Van Steen, E.; Claeys, M.; Dry, M.E.; van de Loosdrecht, J.; Viljoen, E.L.; Visagie, J.L. Stability of nanocrystals: Thermodynamic analysis of oxidation and re-reduction of cobalt in water/hydrogen mixtures. *J. Phys. Chem. B* **2005**, *109*, 3575–3577. [[CrossRef](#)] [[PubMed](#)]
71. Iglesia, E. Design, synthesis, and use of cobalt-based Fischer–Tropsch synthesis catalysts. *Appl. Catal. A Gen.* **1997**, *161*, 59–78. [[CrossRef](#)]
72. Zhang, L.; Chen, K.; Chen, B.; White, J.L.; Resasco, D.E. Factors that determine zeolite stability in hot liquid water. *J. Am. Chem. Soc.* **2015**, *137*, 11810–11819. [[CrossRef](#)]
73. Rostrup-Neilson, J.; Trimm, D.L. Mechanisms of carbon formation on nickel-containing catalysts. *J. Catal.* **1977**, *48*, 155–165. [[CrossRef](#)]
74. Trimm, D.L. The formation and removal of coke from nickel catalyst. *Catal. Rev. Sci. Eng.* **1977**, *16*, 155–189. [[CrossRef](#)]
75. Trimm, D.L. Catalyst design for reduced coking (review). *Appl. Catal.* **1983**, *5*, 263–290. [[CrossRef](#)]
76. Bartholomew, C.H. Carbon deposition in steam reforming and methanation. *Catal. Rev. Sci. Eng.* **1982**, *24*, 67–112. [[CrossRef](#)]
77. Albright, L.F.; Baker, R.T.K. (Eds.) *Coke Formation on Metal Surfaces*; ACS Symposium Series; American Chemical Society: Washington, DC, USA, 1982; Volume 202, pp. 1–200.
78. Menon, P.G. Coke on catalysts-harmful, harmless, invisible and beneficial types. *J. Mol. Catal.* **1990**, *59*, 207–220. [[CrossRef](#)]
79. Chen, D.; Moljord, K.; Holmen, A. Methanol to Olefins: Coke Formation and Deactivation. In *Deactivation and Regeneration of Zeolite Catalysts*; Guisnet, M., Ribeiro, F., Eds.; Imperial College Press: London, UK, 2011; Volume 9, pp. 269–292.
80. Chen, D.; Rebo, H.P.; Grønvold, A.; Moljord, K.; Holmen, A. Methanol conversion to light olefins over SAPO-34: Kinetic modeling of coke formation. *Microporous Mesoporous Mater.* **2000**, *35–36*, 121–135. [[CrossRef](#)]
81. Chen, D.; Moljord, K.; Fuglerud, T.; Holmen, A. The effect of crystal size of SAPO-34 on the selectivity and deactivation of the MTO reaction. *Microporous Mesoporous Mater.* **1999**, *29*, 191–203. [[CrossRef](#)]
82. Nishiyama, N.; Kawaguchi, M.; Hirota, Y.; Van Vu, D.; Egashira, Y.; Ueyama, K. Size control of SAPO-34 crystals and their catalyst lifetime in the methanol-to-olefin reaction. *Appl. Catal. A Gen.* **2009**, *362*, 193–199. [[CrossRef](#)]
83. Müller, S.; Liu, Y.; Vishnuvarthan, M.; Sun, X.; van Veen, A.C.; Haller, G.L.; Sanchez-Sanchez, M.; Lercher, J.A. Coke formation and deactivation pathways on H-ZSM-5 in the conversion of methanol to olefins. *J. Catal.* **2015**, *325*, 48–59. [[CrossRef](#)]
84. Zhou, J.; Gao, M.; Zhang, J.; Liu, W.; Zhang, T.; Li, H.; Xu, Z.; Ye, M.; Liu, Z. Directed transforming of coke to active intermediates in methanol-to-olefins catalyst to boost light olefins selectivity. *Nat. Commun.* **2021**, *12*, 17. [[CrossRef](#)]
85. Yang, M.; Tian, P.; Wang, C.; Yuan, Y.; Yang, Y.; Xu, S.; He, Y.; Liu, Z. A top-down approach to prepare sili-coaluminophosphate molecular sieve nanocrystals with improved catalytic activity. *Chem. Commun.* **2014**, *50*, 1845–1847. [[CrossRef](#)]
86. Xi, D.; Sun, Q.; Chen, X.; Wang, N.; Yu, J. The recyclable synthesis of hierarchical zeolite SAPO-34 with excellent MTO catalytic performance. *Chem. Commun.* **2015**, *51*, 11987–11989. [[CrossRef](#)]
87. Guo, G.; Sun, Q.; Wang, N.; Bai, R.; Yu, J. Cost-effective synthesis of hierarchical SAPO-34 zeolites with abundant intracrystalline mesopores and excellent MTO performance. *Chem. Commun.* **2018**, *54*, 3697–3700. [[CrossRef](#)]
88. Jiang, J.; Wen, C.; Tian, Z.; Wang, Y.; Zhai, Y.; Chen, L.; Li, Y.; Liu, Q.; Wang, C.; Ma, L. Manga-nese-promoted Fe₃O₄ microsphere for efficient conversion of CO₂ to light olefins. *Ind. Eng. Chem. Res.* **2020**, *59*, 2155–2162. [[CrossRef](#)]

89. Witoon, T.; Chaipraditgul, N.; Numpilai, T.; Lapkeatseree, V.; Ayodele, B.; Cheng, C.; Siri-Nguan, N.; Sorn-chamni, T.; Limtrakul, J. Highly active Fe-Co-Zn/K-Al₂O₃ catalysts for CO₂ hydrogenation to light olefins. *Chem. Eng. Sci.* **2021**, *233*, 116428. [CrossRef]
90. Zhang, Z.; Yin, H.; Yu, G.; He, S.; Kang, J.; Liu, Z.; Cheng, K.; Zhang, Q.; Wang, Y. Selective hydrogenation of CO₂ and CO into olefins over sodium- and zinc-promoted iron carbide catalysts. *J. Catal.* **2021**, *395*, 350–361. [CrossRef]
91. Yuan, F.; Zhang, G.; Zhu, J.; Ding, F.; Zhang, A.; Song, C.; Guo, X. Boosting light olefin selectivity in CO₂ hydrogenation by adding Co to Fe catalysts within close proximity. *Catal. Today* **2021**, *371*, 142–149. [CrossRef]
92. Wei, C.; Tu, W.; Jia, L.; Liu, Y.; Lian, H.; Wang, P.; Zhang, Z. The evolutions of carbon and iron species modified by Na and their tuning effect on the hydrogenation of CO₂ to olefins. *Appl. Surf. Sci.* **2020**, *525*, 146622. [CrossRef]
93. Malhi, H.S.; Sun, C.; Zhang, Z.; Liu, Y.; Liu, W.; Ren, P.; Tu, W.; Han, Y.-F. Catalytic consequences of the decoration of sodium and zinc atoms during CO₂ hydrogenation to olefins over iron-based catalyst. *Catal. Today* **2021**, *4*. [CrossRef]
94. Han, Y.; Fang, C.; Ji, X.; Wei, J.; Ge, Q.; Sun, J. Interfacing with carbonaceous potassium promoters boosts catalytic CO₂ hydrogenation of iron. *ACS Catal.* **2020**, *10*, 12098–12108. [CrossRef]
95. Liang, B.; Sun, T.; Ma, J.; Duan, H.; Li, L.; Yang, X.; Zhang, Y.; Su, X.; Huang, Y.; Zhang, T. Mn decorated Na/Fe catalysts for CO₂ hydrogenation to light olefins. *Catal. Sci. Technol.* **2019**, *9*, 456–464. [CrossRef]
96. Yang, S.; Chun, H.; Lee, S.; Han, S.J.; Lee, K.; Kim, Y.T. Comparative study of olefin production from CO and CO₂ Using Na- and K-promoted zinc ferrite. *ACS Catal.* **2020**, *10*, 10742–10759. [CrossRef]
97. Guo, L.; Sun, J.; Ji, X.; Wei, J.; Wen, Z.; Yao, R.; Xu, H.; Ge, Q. Directly converting carbon dioxide to linear α -olefins on bio-promoted catalysts. *Commun. Chem.* **2018**, *1*, 11. [CrossRef]
98. Liang, B.; Duan, H.; Sun, T.; Ma, T.; Liu, X.; Xu, J.; Su, X.; Huang, Y.; Zhang, T. Effect of Na promoter on Fe-based catalyst for CO₂ hydrogenation to alkenes. *ACS Sustain. Chem. Eng.* **2019**, *7*, 925–932. [CrossRef]
99. Ramirez, A.; Gevers, L.; Bavykina, A.; Ould-Chikh, S.; Gascon, J. Metal organic framework-derived iron catalysts for the direct hydrogenation of CO₂ to short chain olefins. *ACS Catal.* **2018**, *8*, 9174–9182. [CrossRef]
100. Zhang, J.; Su, X.; Wang, X.; Ma, Q.; Fan, S.; Zhao, T. Promotion effects of Ce added Fe–Zr–K on CO₂ hydrogenation to light olefins. *React. Kinet. Mech. Catal.* **2018**, *124*, 575–585. [CrossRef]
101. Numpilai, T.; Chanlek, N.; Poo-Arporn, Y.; Cheng, C.K.; Siri-Nguan, N.; Sornchamni, T.; Chareonpanich, M.; Kongkachuichay, P.; Yigit, N.; Rupprechter, G.; et al. Tuning interactions of surface-adsorbed species over Fe-Co/K-Al₂O₃ catalyst by different K content: Selective CO₂ hydrogenation to light olefins. *ChemCatChem* **2020**, *12*, 3306–3320. [CrossRef]
102. Wang, W.; Jiang, X.; Wang, X.; Song, C. Fe–Cu bimetallic catalysts for selective CO₂ hydrogenation to olefin-rich C₂+ hydrocarbons. *Ind. Eng. Chem. Res.* **2018**, *57*, 4535–4542. [CrossRef]
103. Kim, K.Y.; Lee, H.; Noh, W.Y.; Shin, J.; Han, S.J.; Kim, S.K.; An, K.; Lee, J.S. Cobalt ferrite nanoparticles to form a catalytic Co–Fe alloy carbide phase for selective CO₂ hydrogenation to light olefins. *ACS Catal.* **2020**, *10*, 8660–8671. [CrossRef]
104. Boreriboon, N.; Jiang, X.; Song, C.; Prasassarakich, P. Fe-based bimetallic catalysts supported on TiO₂ for selective CO₂ hydrogenation to hydrocarbons. *J. CO₂ Util.* **2018**, *25*, 330–337. [CrossRef]
105. Xu, Q.; Xu, X.; Fan, G.; Yang, L.; Li, F. Unveiling the roles of Fe–Co interactions over ternary spinel-type ZnCo_xFe_{2–x}O₄ catalysts for highly efficient CO₂ hydrogenation to produce light olefins. *J. Catal.* **2021**, *400*, 355–366. [CrossRef]
106. Numpilai, T.; Witoon, T.; Chanlek, N.; Limphirat, W.; Bonura, G.; Chareonpanich, M.; Limtrakul, J. Structure–activity relationships of Fe-Co/K-Al₂O₃ catalysts calcined at different temperatures for CO₂ hydrogenation to light olefins. *Appl. Catal. A Gen.* **2017**, *547*, 219–229. [CrossRef]
107. Rodemerck, U.; Holeña, M.; Wagner, E.; Smejkal, Q.; Barkschat, A.; Baerns, M. Catalyst development for CO₂ hydrogenation to fuels. *ChemCatChem* **2013**, *5*, 1948–1955. [CrossRef]
108. Gong, W.; Ye, R.-P.; Ding, J.; Wang, T.; Shi, X.; Russell, C.K.; Tang, J.; Eddings, E.G.; Zhang, Y.; Fan, M. Effect of copper on highly effective Fe–Mn based catalysts during production of light olefins via Fischer-Tropsch process with low CO₂ emission. *Appl. Catal.* **2020**, *278*, 119302. [CrossRef]
109. Dai, C.; Zhang, A.; Liu, M.; Song, F.; Song, C.; Guo, X. Facile one-step synthesis of hierarchical porous carbon monoliths as superior supports of Fe-based catalysts for CO₂ hydrogenation. *RSC Adv.* **2016**, *6*, 10831–10836. [CrossRef]
110. Hu, S.; Liu, M.; Ding, F.; Song, C.; Zhang, G.; Guo, X. Hydrothermally stable MOFs for CO₂ hydrogenation over iron-based catalyst to light olefins. *J. CO₂ Util.* **2016**, *15*, 89–95. [CrossRef]
111. Raghav, H.; Siva Kumar Konathala, L.N.; Mishra, N.; Joshi, B.; Goyal, R.; Agrawal, A.; Sarkar, B. Fe-decorated hierarchical molybdenum carbide for direct conversion of CO₂ into ethylene: Tailoring activity and stability. *J. CO₂ Util.* **2021**, *50*, 101607. [CrossRef]
112. Huang, J.; Jiang, S.; Wang, M.; Wang, X.; Gao, J.; Song, C. Dynamic evolution of Fe and carbon species over different ZrO₂ supports during CO prerduction and their effects on CO₂ hydrogenation to light olefins. *ACS Sustain. Chem. Eng.* **2021**, *9*, 7891–7903. [CrossRef]
113. Torrente-Murciano, L.; Chapman, R.S.L.; Narvaez-Dinamarca, A.; Mattia, D.; Jones, M.D. Effect of nanostructured ceria as support for the iron catalysed hydrogenation of CO₂ into hydrocarbons. *Phys. Chem. Chem. Phys.* **2016**, *18*, 15496–15500. [CrossRef] [PubMed]
114. Gu, H.; Ding, J.; Zhong, Q.; Zeng, Y.; Song, F. Promotion of surface oxygen vacancies on the light olefins synthesis from catalytic CO₂ hydrogenation over Fe–K/ZrO₂ catalysts. *Int. J. Hydrogen Energy* **2019**, *44*, 11808–11816. [CrossRef]

115. Owen, R.E.; Pluckinski, P.; Mattia, D.; Torrente-Murciano, L.; Ting, V.; Jones, M.D. Effect of support of Co-Na-Mo catalysts on the direct conversion of CO₂ to hydrocarbons. *J. CO₂ Util.* **2016**, *16*, 97–103. [[CrossRef](#)]
116. Wang, P.; Zha, F.; Yao, L.; Chang, Y. Synthesis of light olefins from CO₂ hydrogenation over (CuO-ZnO)-kaolin/SAPO-34 molecular sieves. *Appl. Clay Sci.* **2018**, *163*, 249–256. [[CrossRef](#)]
117. Wang, S.; Zhang, L.; Zhang, W.; Wang, P.; Qin, Z.; Yan, W.; Dong, M.; Li, J.; Wang, J.; He, L.; et al. Selective conversion of CO₂ into propene and butene. *Chem* **2020**, *6*, 3344–3363. [[CrossRef](#)]
118. Li, W.; Wang, K.; Zhan, G.; Huang, J.; Li, Q. Design and synthesis of bioinspired ZnZrOx & bio-ZSM-5 inte-grated nanocatalysts to boost CO₂ hydrogenation to light olefins. *ACS Sustain. Chem. Eng.* **2021**, *9*, 6446–6458.
119. Wang, S.; Wang, P.; Qin, Z.; Yan, W.; Dong, M.; Li, J.; Wang, J.; Fan, W. Enhancement of light olefin produc-tion in CO₂ hydrogenation over In₂O₃-based oxide and SAPO-34 composite. *J. Catal.* **2020**, *391*, 459–470. [[CrossRef](#)]
120. Chen, J.; Wang, X.; Wu, D.; Zhang, J.; Ma, Q.; Gao, X.; Lai, X.; Xia, H.; Fan, S.; Zhao, T. Hydrogenation of CO₂ to light olefins on CuZnZr@(Zn-)SAPO-34 catalysts: Strategy for product distribution. *Fuel* **2019**, *239*, 44–52. [[CrossRef](#)]
121. Liu, X.; Wang, M.; Yin, H.; Hu, J.; Cheng, K.; Kang, J.; Zhang, Q.; Wang, Y. Tandem catalysis for hydrogena-tion of CO and CO₂ to lower olefins with bifunctional catalysts composed of spinel oxide and SAPO-34. *ACS Catal.* **2020**, *10*, 8303–8314. [[CrossRef](#)]
122. Tong, M.; Chizema, L.G.; Chang, X.; Hondo, E.; Dai, L.; Zeng, Y.; Zeng, C.; Ahmad, H.; Yang, R.; Lu, P. Tan-dem catalysis over tailored ZnO-ZrO₂/MnSAPO-34 composite catalyst for enhanced light olefins selectivity in CO₂ hydrogenation. *Microporous Mesoporous Mater.* **2021**, *320*, 111105. [[CrossRef](#)]
123. Wang, X.; Wu, D.; Zhang, J.; Gao, X.; Ma, Q.; Fan, S.; Zhao, T. Highly selective conversion of CO₂ to light ole-fins via Fischer-Tropsch synthesis over stable layered K-Fe-Ti catalysts. *Appl. Catal. A Gen.* **2019**, *573*, 32–40. [[CrossRef](#)]
124. Elishav, O.; Shener, Y.; Beilin, V.; Langau, M.V.; Herskowitz, M.; Shter, G.E.; Grader, G.S. Electrospun Fe–Al–O nanobelts for selective CO₂ hydrogenation to light olefins. *ACS Appl. Mater. Interfaces* **2020**, *12*, 24855–24867. [[CrossRef](#)] [[PubMed](#)]
125. Chen, H.; Liu, P.; Li, J.; Wang, Y.; She, C.; Liu, J.; Zhang, L.; Yang, Q.; Zhou, S.; Feng, X. MgH₂/Cu_xO hydrogen storage composite with defect-rich surfaces for carbon dioxide hydrogenation. *ACS Appl. Mater. Interfaces* **2019**, *11*, 31009–31017. [[CrossRef](#)] [[PubMed](#)]
126. Tian, H.; Yao, J.; Zha, F.; Yao, L.; Chang, Y. Catalytic activity of SAPO-34 molecular sieves prepared by using palygorskite in the synthesis of light olefins via CO₂ hydrogenation. *Appl. Clay Sci.* **2020**, *184*, 105392. [[CrossRef](#)]
127. Wu, T.; Lin, J.; Cheng, Y.; Tian, J.; Wang, S.; Xie, S.; Pei, Y.; Yan, S.; Qiao, M.; Xu, H.; et al. Porous gra-phene-confined Fe–K as highly efficient catalyst for CO₂ direct hydrogenation to light olefins. *ACS Appl. Mater. Interfaces* **2018**, *10*, 23439–23443. [[CrossRef](#)]
128. Chen, H.; Liu, J.; Liu, P.; Wang, Y.; Xiao, H.; Yang, Q.; Feng, X.; Zhou, S. Carbon-confined magnesium hydride nano-lamellae for catalytic hydrogenation of carbon dioxide to lower olefins. *J. Catal.* **2019**, *379*, 121–128. [[CrossRef](#)]
129. Fujiwara, M.; Satake, T.; Shiokawa, K.; Sakurai, H. CO₂ hydrogenation for C₂+ hydrocarbon synthesis over composite catalyst using surface modified HB zeolite. *Appl. Catal. B Environ.* **2015**, *179*, 37–43. [[CrossRef](#)]
130. Tan, L.; Wang, F.; Zhang, P.P.; Suzuki, Y.; Wu, Y.; Chen, J.; Yang, G.; Tsubaki, N. Design of a core–shell catalyst: An effective strategy for suppressing side reactions in syngas for direct selective conversion to light olefins. *Chem. Sci.* **2020**, *11*, 4097–4105. [[CrossRef](#)] [[PubMed](#)]